Energy Resolution of a Liquid Argon Electromagnetic Calorimeter with Pointing Accordion Geometry

by

Steven H. Robertson
B.Sc.(Pure Mathematics), University of Calgary, Calgary, Alberta, Canada, 1992.
B.Sc. (Physics), University of Calgary, Calgary, Alberta, Canada, 1990.

A thesis submitted in partial fulfillment
of the requirements for the degree of
Master of Science
in the Department of Physics and Astronomy.

We accept this thesis as conforming
to the required standard.

Dr. M. Lefebvre, Supervisor (Department of Physics and Astronomy)

Dr. A. Astbury, Departmental Member (Department of Physics and Astronomy)

Dr. D. Harrington, Outside Member (Department of Chemistry)

Dr. C. Oram, External Examiner (TRIUMF)

Supervisor: Dr. M. Lefebvre

Abstract

The RD3 collaboration has constructed and tested a number of liquid argon electromagnetic calorimeter prototypes with LHC performance specifications. These calorimeters combine a novel accordion geometry with a fast readout scheme, resulting in low pileup radiation hard devices with high granularity and minimal dead space. A pointing geometry barrel calorimeter prototype was recently tested at the CERN SPS using electron beams with energy 10 GeV to 287 GeV. The energy response of the calorimeter was found to vary with the electron impact point with an rms of $\sim$ 0.5%. After applying position dependent response corrections and optimizing the energy weighting with respect to the longitudinal segmentation, an energy resolution of $(0.40 \pm 0.07)\% \oplus (10.2 \pm 0.6)\%/\sqrt{E} \oplus (0.33 \pm 0.02)/E$ (where E is in GeV) and a large scale response uniformity of $0.61\% \pm 0.05\%$ were obtained for this prototype at $\eta = 0.11$ with a readout time of $\sim$ 35 ns.

Examiners:

Dr. M. Lefebvre, Supervisor (Department of Physics and Astronomy)

Dr. A. Astbury, Departmental Member (Department of Physics and Astronomy)

Dr. D. Harrington, Outside Member (Department of Chemistry)

Dr. C. Oram, External Examiner (TRIUMF)

Contents

List of Tables

List of Figures

Chapter 1

Introduction

The European Centre for Particle Physics (CERN) is proposing to build a pp collider which will be able to probe nature at energies exceeding those of currently existing particle accelerators. The Large Hadron Collider (LHC) [1] will permit two proton beams to collide with a centre of mass energy of 14 TeV[1]. The high luminosity (10^{34} cm^{-2}s^{-1}) which is necessary to detect signatures of very low cross section processes such as the production and decay of Standard Model Higgs bosons imposes challenging requirements on the detectors to be used at the LHC. The ATLAS collaboration is proposing a general purpose detector which has the capacity to exploit the full discovery potential of the LHC. A Letter of Intent [2] was submitted in October 1992, and a Technical Proposal will be submitted in December 1994.

The RD3 collaboration [3] has been developing fast calorimetry techniques utilizing a liquid argon (LAr) active medium which are suitable for use in the ATLAS detector at the LHC [4, 5, 6, 7]. These devices provide energy measurements of leptons and hadrons, as well as assisting in position reconstruction and particle identification. The RD3 calorimeters utilize a novel "accordion" geometry combined with a fast readout scheme, resulting in low

[1] The natural units $\hbar = c = 1$ are used in this thesis unless otherwise specified.

pileup radiation hard and hermetic devices that can provide precision energy measurements in the high luminosity LHC environment. Several prototype calorimeters have been tested at CERN since 1990 [8, 9, 10, 11, 12].

This thesis presents an analysis of the electron energy resolution of a pointing accordion geometry LAr electromagnetic calorimeter prototype [13] using data from beam tests which took place at the CERN SPS during the spring and autumn of 1993. Chapter 2 describes the interactions of energetic particles with matter and how these processes relate to calorimetry. The LHC and the ATLAS detector are introduced in Chapter 3. The RD3 pointing geometry calorimeter prototype is described in detail in chapter 4, and an analysis of the electron energy resolution is presented in chapter 5.

Chapter 2

Calorimetry

2.1 Particle Interactions with Matter

An electromagnetic (EM) calorimeter is a device that measures the energy of particles that interact primarily through the EM force, particularly electrons and photons. Such a device can also be used to distinguish electrons and photons from muons or hadrons by exploiting the differences in the way that these particles interact with matter. When electromagnetically interacting particles pass though matter they deposit energy in the medium by a number of processes. At the energy scale of interest at the LHC the dominant interaction between photons and matter is *pair production*. This is the conversion of a photon into an e^+e^- pair through an interaction with the electric field of a nucleus in the material. Charged particles interact with matter through ionization, bremsstrahlung, elastic and inelastic scattering from atomic nuclei and the emission of Cherenkov radiation. Only the first two of these will be considered here [14]. Energy loss by ionization is described by the Bethe-Bloch equation [15], which expresses the average energy deposition per unit path length (dE/dx) in terms of the particle energy,

$$-\frac{dE}{dx} = 4\pi N_a r_e^2 m_e \frac{Z}{A}\frac{z^2}{\beta^2}\left[ln\left(\frac{2m_e\gamma^2\beta^2}{I}\right) - \beta^2 - \frac{\delta}{2}\right] \quad , \tag{2.1}$$

where N_a is Avogadro's number, $r_e = 2.817 \times 10^{-13}$ cm is the classical electron radius, m_e is the mass of the electron (in eV), Z and A are respectively the atomic number and weight of the the absorbing material, z is the charge of the incident particle in units of e, β is the velocity of the incident particle as a fraction of the speed of light, $\gamma = 1/\sqrt{1-\beta^2}$, I is the ionization constant ($\simeq 10\,Z^{0.9}$ eV for $Z > 1$), and δ is the density correction factor. This function drops rapidly with increasing particle energy, reaching a minimum at about $\beta = 0.96$ then increases slowly due to relativistic effects. A particle with energy at this minimum is called a *minimum ionizing particle* and typically deposits ~ 1 to $2\,\mathrm{MeV/g{\cdot}cm^{-2}}$ in the medium.

For a heavy charged particle such as a muon, ionization is the primary source of energy loss for the particle energies considered at the LHC. Less massive particles such as electrons have a significant cross section for higher order EM interactions with matter at these energies. For example, a particle may be scattered by the electric field of nuclei in the material, radiating a photon in the process. This process is known as *bremsstrahlung.* Energetic electrons and positrons can radiate many hard bremsstrahlung photons before being stopped in the material. The cross section for photon radiation depends on the inverse square of the particle mass, so this process is supressed by a factor of about 40 000 for muons as compared to electrons.

When an energetic electron passes through matter it will radiate bremsstrahlung photons and suffer energy losses due to ionization and scattering until it is stopped by the medium. If these photons are sufficiently energetic they will pair produce, resulting in more charged particles that can in turn radiate bremsstrahlung photons. This produces a cascade of particles known as an *electromagnetic shower* [16]. Particle multiplication by the processes of pair production and bremsstrahlung will occur until the average energy of the particles in the shower drops below the *critical energy* (ϵ_c) characteristic of the material. The critical energy is defined to be the electron energy at which the energy losses due to radiation equal the energy losses by ionization, and it is given approximately by the formula

$\epsilon_c \simeq 800$ MeV $/(Z + 1.2)$. Above ϵ_c a photon will produce more than one charged particle on average, and electrons will typically radiate one or more photons.

The characteristics of an EM shower are sensitive to the electron density in the medium, which is roughly proportional to the average atomic number (Z) of the material. The longitudinal and transverse dimensions of an EM shower can be conveniently described in terms of two approximately material independent quantities. The *radiation length* (X_0) characterizes the longitudinal shower dimensions, and is defined to be the average distance over which an energetic ($> 1\,\mathrm{GeV}$) electron will radiate $(1 - 1/e)$ (63%) of its energy by bremsstrahlung. A very energetic photon will travel a distance of $9/7\,X_0$ on average before pair producing. The transverse spread of an EM shower is due to multiple scattering of electrons away from the shower axis, the angle between electrons and positrons produced by pair production, and bremsstrahlung photons emitted away from the shower axis. The most natural unit to describe this width is the spread of an electron beam with incident energy ϵ_c which has penetrated a distance X_0 of material. This unit is known as the *Molière radius* (ρ_m), and is defined by $\rho_m = E_s X_0/\epsilon_c$, where $E_s = m_e\sqrt{4\pi/\alpha} \simeq 21\,\mathrm{MeV}$. More than 90% of the energy of a shower is contained within a cylinder of radius $2\rho_m$.

A simple model of an EM shower can be obtained by considering the total number N of particles present in a shower after t radiation lengths of material to be given by $N \simeq 2^t$. The average energy of each particle is $E(t) \simeq E_0/2^t$, where E_0 is the energy of the electron or photon which initiates the shower. Once the average particle energy drops below ϵ_c, fewer particles are produced than are absorbed by the medium and so particle multiplication ceases. The maximum number of particles present in a shower is therefore $N_{\max} \simeq E_0/\epsilon_c$. Assuming that the shower ends when the average particle energy drops below ϵ_c, the penetration depth of the shower $t_{\max}$ is given by the expression $E(t_{\max}) = E_0/2^{t_{\max}} = \epsilon_c$. Solving for $t_{\max}$ gives

$$t_{\max} = \frac{\ln(E_0/\epsilon_c)}{\ln 2} \quad . \tag{2.2}$$

The penetration depth therefore scales as the logarithm of the particle energy. Experimentally, the term in the denominator is found to be approximately equal to one rather than $\ln 2$. Typically $\sim 25\ X_0$ are required to contain 95% of the energy of a 100 GeV EM shower.

2.2 Electromagnetic Calorimetry

Each charged particle in an EM shower will lose energy through ionization of the medium, producing a large number of ion-electron pairs that can be used to produce a measurable signal. Although not all of the shower energy is deposited in the form of ionization, the measurable signal will be proportional to the energy of the incident particle as long as the shower is fully contained. Thus the energy of the incident particle can be reconstructed by measuring the signal produced by a fully contained EM shower. Such a device is known as a *homogeneous calorimeter.* A *sampling calorimeter* consists of alternate layers of an active medium and a passive absorber such that only a fraction of the shower is sampled. Only the measurable signal produced in the active medium is collected and used to reconstruct the incident particle energy. The fraction of the shower energy which produces a measurable signal in the active medium is referred to as the *sampling fraction* (η_s). The denser absorbing medium serves to reduce the physical thickness of the calorimeter necessary to fully contain the shower. The number of active layers per radiation length of material is denoted the *sampling frequency.* The energy resolution of such a device will be dominated by *sampling fluctuations*, which arise from statistical variations in the measurable signal collected at each active layer [17]. These fluctuations are proportional to the number (n) of particle tracks crossing active layers, where n has a Poisson distribution with a variance $\sqrt{n}$. Since the measured energy of a shower is proportional to n, sampling fluctuations contribute to the energy resolution $\sigma(E)/E$ of the calorimeter, yielding

$$\frac{\sigma(E)}{E} \propto \frac{1}{\sqrt{E}} \quad . \tag{2.3}$$

The energy resolution of a sampling calorimeter therefore improves as the shower energy increases. The resolution of a real sampling calorimeter is conveniently expressed as the quadratic sum of three terms [2]:

$$\frac{\sigma(E)}{E} = a \oplus \frac{b}{\sqrt{E}} \oplus \frac{c}{E} \quad . \tag{2.4}$$

The constant term a is associated with mechanical imperfections of the calorimeter, quality of the detection medium, shower leakage, cell to cell calibration, uniformity of response and stability with time. At high energies this term will dominate the energy resolution. At lower energies the sampling term $b/\sqrt{E}$ becomes significant. The noise term c/E is associated with electronics noise and noise due to event pileup in a high rate environment, and dominates the energy resolution at low energies.

2.3 Liquid Argon Calorimeters

The measurable signal produced in a calorimeter can take a number of forms, one of which is an electric current produced by the drift of ionization charge in the active layers of the calorimeter. In calorimeters which utilize this technique, recombination effects have restricted the choices of suitable active media to a number of gases and a few liquids. The principal problem is the presence of electronegative impurities such as oxygen which can absorb ionization electrons. Sampling calorimeters utilizing a liquid active medium possess a higher density and therefore produce a larger number of ion-electron pairs per unit length than gas calorimeters, however liquids are also much more difficult to purify. Because argon is a chemically inert noble gas, it is relatively easy to maintain its purity to the required level of typically a few parts per million of O_2. It is also inexpensive, readily available and can be easily cooled below its boiling point (87.45 K) using liquid nitrogen.

A simplified LAr calorimeter "cell" consists of a liquid argon filled gap, bounded on two sides by absorber layers. A readout electrode layer is placed in the middle of the gap

and a high voltage is applied to the electrode relative to the absorbers in order to produce an electric field in the gap. An ionizing particle traversing the LAr gap in a direction perpendicular to the plates creates a "straw" of ion-electron pairs that drift towards the readout electrodes under the influence of the applied electric field. The charge Q that is produced by a particle of initial energy E is approximately given by

$$Q = \frac{\eta_s}{W_i} E \tag{2.5}$$

where $W_i = 26$ eV is the mean energy for ion-electron pair creation in argon [18]. These charges are collected at the readout electrodes, producing a current waveform with a triangular shape:

$$i(t) = \frac{Q}{t_{\text{drift}}} \left[1 - \frac{t}{t_{\text{drift}}} \right] \tag{2.6}$$

where $t_{\text{drift}} = d/v_e$, d is the gap thickness and v_e is the drift velocity [19]. For an electric field of $\sim 1\,\text{kV/mm}$ the drift time in a 2 mm LAr gap is about 400 ns. This current pulse is amplified and can be used, along with the signal from other cells, to reconstruct the energy of the incident particle.

Chapter 3

ATLAS and the LHC

3.1 The Standard Model

The fundamental interactions between particles are described by a highly successful theory known as the Standard Model (SM) [20]. In this theory, matter is composed of point-like spin 1/2 fermions which interact via the strong, weak and EM forces. The gravitational force is sufficiently weak at the length and mass scales of interest to particle physics that it is neglected here. These fundamental forces are mediated by the exchange of particles known as gauge bosons. Some properties of the fermions and bosons are listed in Table 3.1.

Fermions can be catagorized as leptons or quarks based on their ability to interact via the strong force. Leptons consist of the electron, muon, tau and their associated neutrinos. They possess integer charge and interact only via the weak and EM forces. The six quarks (u, d, s, c, t, and b) all possess fractional charges and are able to interact by the strong force as well as the weak and EM forces. Because of the nature of the strong interaction quarks have never been observed to exist in isolation, appearing only in bound states of two or three quarks known respectively as mesons and baryons. Each fermion has an associated

Fermions (spin = 1/2)

Leptons			Quarks		
Flavour	Charge	Mass (GeV)	Flavour	Charge	Mass (GeV)
ν_e	0	$< 2 \times 10^{-8}$	u	$+2/3$	$\sim 4 \times 10^{-3}$
e	-1	5.1×10^{-4}	d	$-1/3$	$\sim 7 \times 10^{-3}$
ν_μ	0	$< 3 \times 10^{-4}$	c	$+2/3$	~ 1.5
μ	-1	0.106	s	$-1/3$	~ 0.15
ν_τ	0	$< 4 \times 10^{-2}$	t	$+2/3$	~ 174
τ	-1	1.784	b	$-1/3$	~ 4.7

Bosons (spin = 1)

Name	Charge	Mass (GeV)
photon (γ)	0	0
Z^0	0	91.16
W^+	$+1$	80.6
W^-	-1	80.6
gluon (g)	0	0

Table 3.1: Properties of the fermions and bosons in the Standard Model [15]. The discovery of the top quark (t) has not yet been confirmed [22].

antiparticle with the opposite electric charge. With recent evidence for the top (t) quark from CDF at Fermilab [22], all of the fermions predicted by the Standard Model with the exception of the tau neutrino (ν_τ), are believed to have been directly observed.

The leptons and quarks are each divided into doublets based on the preference of the weak force to convert members of the doublets into one another by charged current interactions. This division into doublets effectively divides the fermions into three families, each consisting of a pair of quarks with charges $+2/3$ and $-1/3$, a charged lepton and a neutrino. Ordinary matter is composed only of members of the first family (u, d, e and ν_e), while the remaining fermions can only be observed in particle accelerators and cosmic ray experiments. Charged current interactions which convert quarks from one doublet into members of another doublet also occur, but with a lower probability. This mixing between families occurs because quark mass eigenstates are "rotated" relative to the weak interaction eigenstates, and is described by the CKM matrix [21]. Mixing between families is not observed in the lepton sector because the absence of neutrino masses guarantee that the weak eigenstates and mass eigenstates are identical. Neutral current processes which change a fermion's identity ("flavour") are not permitted by the SM.

The couplings between fermions are the result of the invariance of the SM under a class of symmetry transformations known as local gauge transformations. These are described by the group structure $SU(3)_C \times SU(2)_L \times U(1)_Y$, where the $SU(3)_C$ group describes the couplings between strongly interacting particles by the exchange of colour carrying gauge bosons called gluons, and the remaining two terms describe the unified electroweak interaction of Glashow, Weinberg and Salam [23]. The $SU(2)_L \times U(1)_Y$ symmetry of the electroweak interaction is spontaneously broken to $U(1)_Q$ (where Q is the electric charge) by the introduction of a scalar Higgs field. This field is required in order to generate particle masses in the SM in a gauge invariant, Lorentz invariant and renormalizable way, but also yields a massive scalar particle known as the Higgs boson [24]. This particle has yet to be observed, and because of the nature of the Higgs mechanism there are only broad bounds

on its mass. After symmetry breaking the electroweak force becomes the separate EM and weak forces. A massless, neutral gauge boson called the photon (γ) is associated with the EM interaction, while the remaining three gauge bosons, $W^{\pm}$ and Z^0, are associated with the weak interaction. The apparent weakness of the weak force relative to the EM force is due to the large masses of these particles (see table 3.1). The $W^{\pm}$ and Z^0 bosons were discovered at CERN in 1982 [25, 26, 27, 28]. Since then the masses and couplings of the W's have been measured by UA2 and CDF [15] and precision measurements of the Z^0 have been made at LEP [29], providing stringent tests of the SM.

The SM has proven to be capable of precisely predicting a broad spectrum of particle physics phenomena, however it is not expected to stand up to scrutiny at the TeV energy scale. Extensions of the minimal SM predict the existence of multiple Higgs bosons as well as numerous other unobserved particles. Understanding of symmetry breaking in the electroweak sector and the origin of mass are challenges that are to be addressed by future high energy hadron colliders such as the LHC.

3.2 Physics Processes at the LHC

The primary purpose of the LHC is to understand the origin of mass and to explore physics beyond the SM. The production and detection of Higgs bosons is therefore one of the benchmark processes for which the LHC is designed. A SM Higgs boson is expected to be produced at a pp collider by a number of processes, of which gluon fusion ($gg \rightarrow H^0$) through top quark loops, and intermediate vector boson fusion ($qq \rightarrow H^0qq$) are the dominant channels [30]. The total Higgs cross section is dependent on the masses of the Higgs and the top quark, but is expected to be $\sim 10^{-2}$ nb at the the energy of the LHC. Because of this small cross section it will be necessary to operate at high luminosity and have a high detector efficiency. The mass of the Higgs boson is not predicted by theory, so experiments must

Higgs decay channel	Mass range
$H^0 \longrightarrow \gamma\gamma$	80 GeV $< m_H <$ 200 GeV
$H^0 \longrightarrow ZZ^* \longrightarrow 4l$	130 GeV $< m_H < 2m_Z$
$H^0 \longrightarrow ZZ, W^+W^-$	$2m_Z < m_H <$ 800 GeV
$\longrightarrow 4l^{\pm}$	
$\longrightarrow l\nu +$ 2 jets	
$\longrightarrow l^+l^- +$ 2 jets	
$\longrightarrow l^+l^- + \nu\bar{\nu}$	

Table 3.2: Some of the Higgs boson decay channels which are potentially observable in various Higgs mass ranges. l represents either electrons or muons.

be designed with the ability to detect signatures of several potential Higgs decay channels which are available in different mass ranges. Some of these channels are listed in Table 3.2. For a low to intermediate mass Higgs boson ($m_H < 200$ GeV), the most promising channel is the decay to two photons, where the Higgs is either produced directly or in association with a Z, W or a $t\bar{t}$ pair. In the later case, the event can be tagged using charged leptons produced by the decay of the associated particle. A second channel that is available in the intermediate mass range is the decay into a virtual Z pair, which can produce a very clean four lepton signature. If the Higgs boson is more than twice the mass of the Z, real Z and W pairs can be produced, which will decay to combinations of charged leptons, neutrinos and jets as shown in the table.

Two other avenues of research that will be available at the LHC are searches for particles beyond the scope of the SM [2], and for signatures of top quark decays. The LHC is expected to produce on the order of 25 000 $t\bar{t}$ pairs per day by the dominant production process $gg \rightarrow t\bar{t}$, even at low luminosity running (10^{33} cm^{-2}s^{-1}), allowing precise measurements to be made of the top quark mass and decays. By using a single lepton trigger on the decay $t \rightarrow Wb$ where the W decays to $l\nu$, the inclusive decays of the other top quark can be studied [31].

3.3 The ATLAS Detector

The ATLAS Collaboration is designing a general purpose detector for the LHC which is capable of exploiting its full physics potential. The layout of the ATLAS detector is shown in figure 3.1. The detector geometry can be most conveniently described in terms of a spherical coordinate system, in which the beam axis is denoted z, the azimuthal angle is ϕ and the polar angle is θ. It is also convenient to define the *pseudorapidity* η

$$\eta \equiv -\ln \tan\left(\frac{\theta}{2}\right) \quad . \tag{3.1}$$

Because of the diversity of the final state signatures to which ATLAS will need to be sensitive, equal emphasis is placed on the detection of photons, charged leptons, hadrons, and jet and missing energy measurements. The inner detector must provide efficient tracking for heavy flavour tagging during low luminosity running, and also aid lepton and photon identification and lepton momentum measurement at high luminosities. Charge tracks are bent by a 2 T magnetic field produced by a superconducting solenoid imbedded in the inner wall of the EM calorimeter cryostat. Precision photon and electron energy measurements are provided by the EM calorimeter. The required performance of the ATLAS EM calorimeter will be discussed in the following section. The hadronic calorimeter complements the EM calorimeter by providing hermetic hadron and jet energy measurements, allowing missing E_T measurements to be made. The three layer muon system provides precise, stand-alone measurements of muon momentum, which can be combined with information from the inner tracker to improve momentum measurements even further. An air-core toroid magnet system produces a field which bends particle paths in the z direction to permit measurements of the muon momentum. This magnet system minimizes the amount of material through which muons must travel, reducing multiple scattering and therefore improving the muon momentum resolution.

3.4 Calorimetry Requirements

The high luminosity (10^{34} cm^{-2}s^{-1}) which is required in order to detect signatures of very low cross section processes such as the production and decay of SM Higgs bosons imposes challenging requirements on EM calorimeters to be used at the LHC. The LHC will have a bunch crossing time of 25 ns with an average of about 18 events occurring per bunch crossing. The ATLAS calorimeters will therefore need a fast response (about 20 to 100 ns) to physics signals in order to maximize detector efficiency and maintain an acceptable level of noise due to event pileup. They must be radiation hard in order to withstand doses on the order of 10^4 Gy and 10^{14} n/cm^2 expected over the full lifetime of the ATLAS experiment [2]. Good hermeticity and acceptance over a large pseudorapidity interval ($\eta_{\max} \geq 2.5$) are required for missing transverse energy measurements to identify non-interacting particles. Fine granularity ($\triangle\phi \times \triangle\eta \approx 0.02 \times 0.02$ where $\triangle\phi$ is the cell size in radians in the direction perpendicular to the beam axis and $\triangle\eta$ is the cell size in pseudorapidity units parallel to the beam axis) is necessary in order to reduce event pileup and provide accurate measurements of shower positions. The EM calorimeter must be capable of energy measurements over a large dynamic range (a few GeV to about 3 TeV) with good energy resolution ($a \leq 1\%$ and $b \leq 10\%$ GeV$^{1/2}$ in equation 2.4) [2]. The large scale energy resolution of the calorimeter is sensitive to cell to cell response variations and to response fluctuations with time. To achieve the required response uniformity of better than 1% over large areas, the ATLAS calorimeters must meet precise mechanical tolerances, possess reliable readout electronics and possess an easy method of intercalibrating the large number ($\sim 10^6$) of electronic channels.

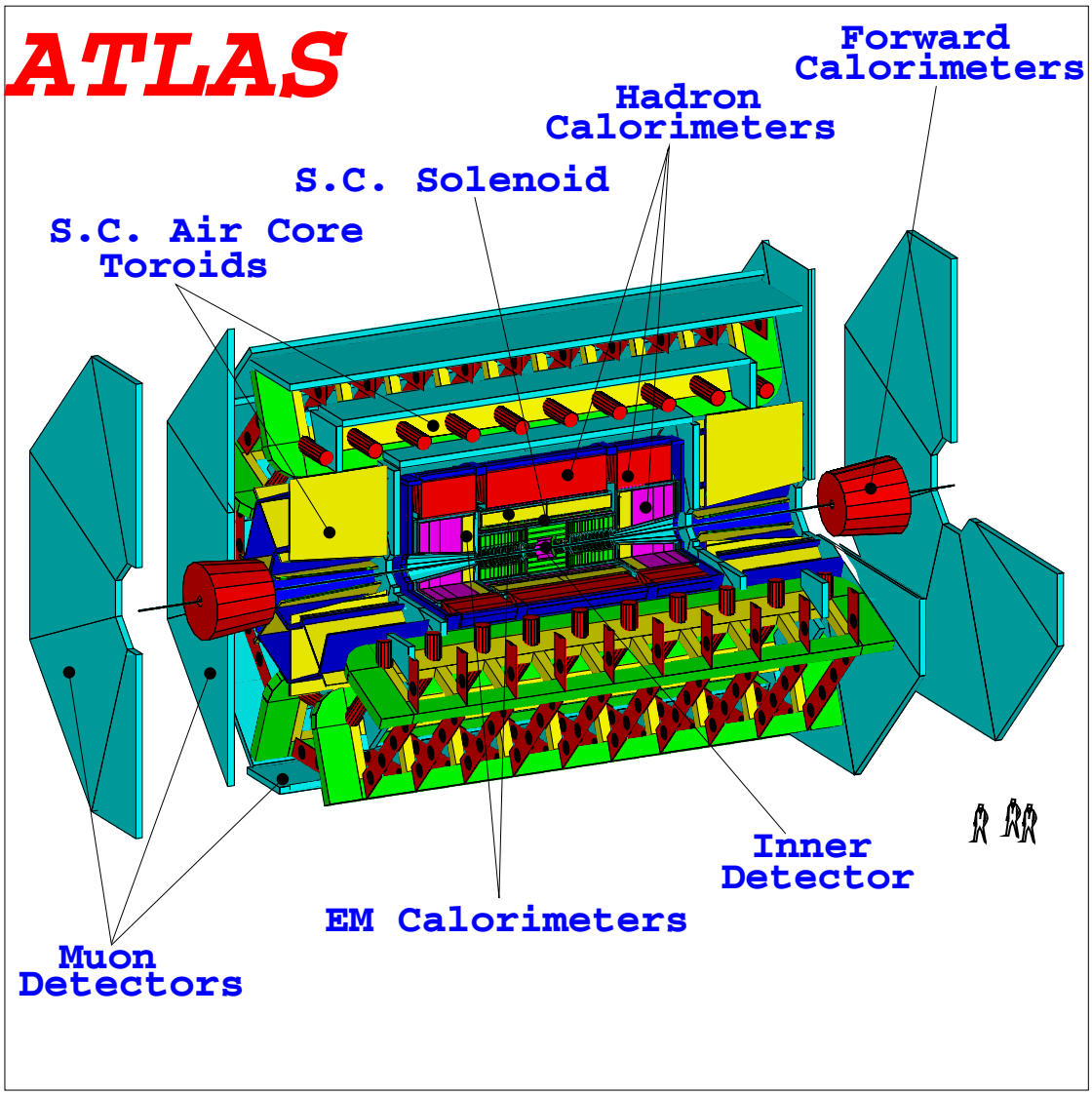

Figure 3.1: Schematic diagram of the ATLAS detector showing the detector subcomponents. The figures to the right provide the scale.

Chapter 4

The Accordion Calorimeter

4.1 The Accordion Geometry

Conventional LAr calorimeters are limited with regards to their use at the LHC by two main problems: readout speed and hermeticity. The RD3 group has been developing a design for a fast LAr sampling calorimeter incorporating a novel accordion geometry and a fast readout scheme which effectively address these two difficulties. The accordion geometry will be described in this section, while the readout scheme will be discussed in section 4.2. The conventional parallel-plate calorimeter geometry and an accordion geometry are compared in figure 4.1. With a parallel geometry, absorber and readout plates are oriented perpendicular to the direction of the incident particles. The signal on the readout electrodes induced by the drifting charges is brought out of the calorimeter by means of cables running between towers of plates. In an accordion calorimeter, readout electrodes and absorber plates are bent into a zig-zag shape and oriented parallel to the incident particle direction. A shower therefore crosses the same plate repeatedly rather than a series of separate plates (see figure 4.2). Connections to the readout electrodes are made directly at the front and rear faces of the calorimeter, and readout towers are formed automatically by ganging a number (in this case

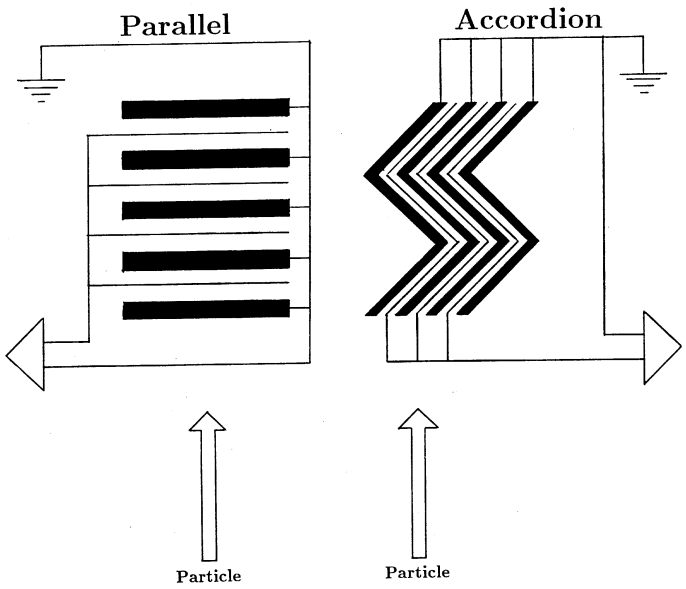

Figure 4.1: Schematic diagram of a conventional parallel plate calorimeter and an accordion geometry calorimeter

three) of adjacent electrodes. This eliminates cracks between towers and reduces the charge transfer time to the preamplifiers by shortening readout lines and reducing the inductance of a calorimeter cell.

4.2 Fast Readout Scheme

The speed of conventional LAr calorimeters is limited by the long drift time in the liquid argon gaps. For a gap size of 1.9 mm and an applied voltage of 2 kV the drift time is about 400 ns. Charge integration times of this length would result in an unacceptable rate of event pileup in the high rate environment of the LHC. However, it is possible to exploit the fast risetime of the ionization current as shown in figure 4.3a. The intrinsic risetime of the ionization current is determined by the time required for the formation of the shower

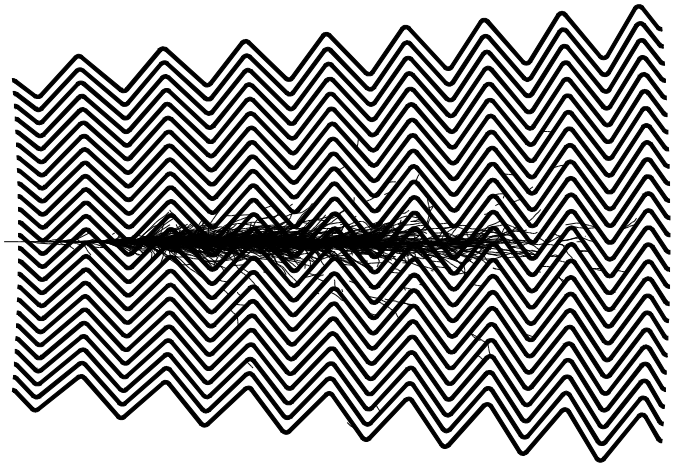

Figure 4.2: GEANT [32] simulation of a 90 GeV electron shower in an accordion EM calorimeter with pointing geometry. Only charge tracks greater than 10 MeV are shown.

($\sim 1\,\mathrm{ns}$). The amplitude of the initial current is found from equation 2.6 to be

$$i(0) = \frac{Q}{t_{\mathrm{drift}}} \tag{4.1}$$

which is proportional to the total ionization charge Q. The signal can be effectively clipped using a bipolar shaper following the charge sensitive preamplifier. The shaper is designed to have a bipolar impulse response with a peaking time $t_p(\delta) \approx 20\,\mathrm{ns}$ (figure 4.3b). A triangular current pulse applied to the shaper results in a pulse as shown in figure 4.3c, with a peaking time $t_p \approx 2t_p(\delta) \approx 35\,\mathrm{ns}$. This peaking time was selected to simultaneously optimize the noise contributions from event pileup in the LHC environment and the electronics [33]. The amplitude of the shaper output is directly proportional to the total charge Q and hence to the incident particle energy. This fast shaping is only effective if the charge transfer time from the readout cell to the preamplifier is at least as fast. The charge transfer time (91%) is minimized by achieving the critical damping condition [34]

$$R = 2\sqrt{\frac{L}{C}} \quad , \tag{4.2}$$

where R is the preamplifier input resistance and L and C are the inductance and capacitance of the elements of a readout cell. The charge transfer time then becomes $4\sqrt{LC}$. It is therefore essential to reduce LC and to select suitable preamplifiers.

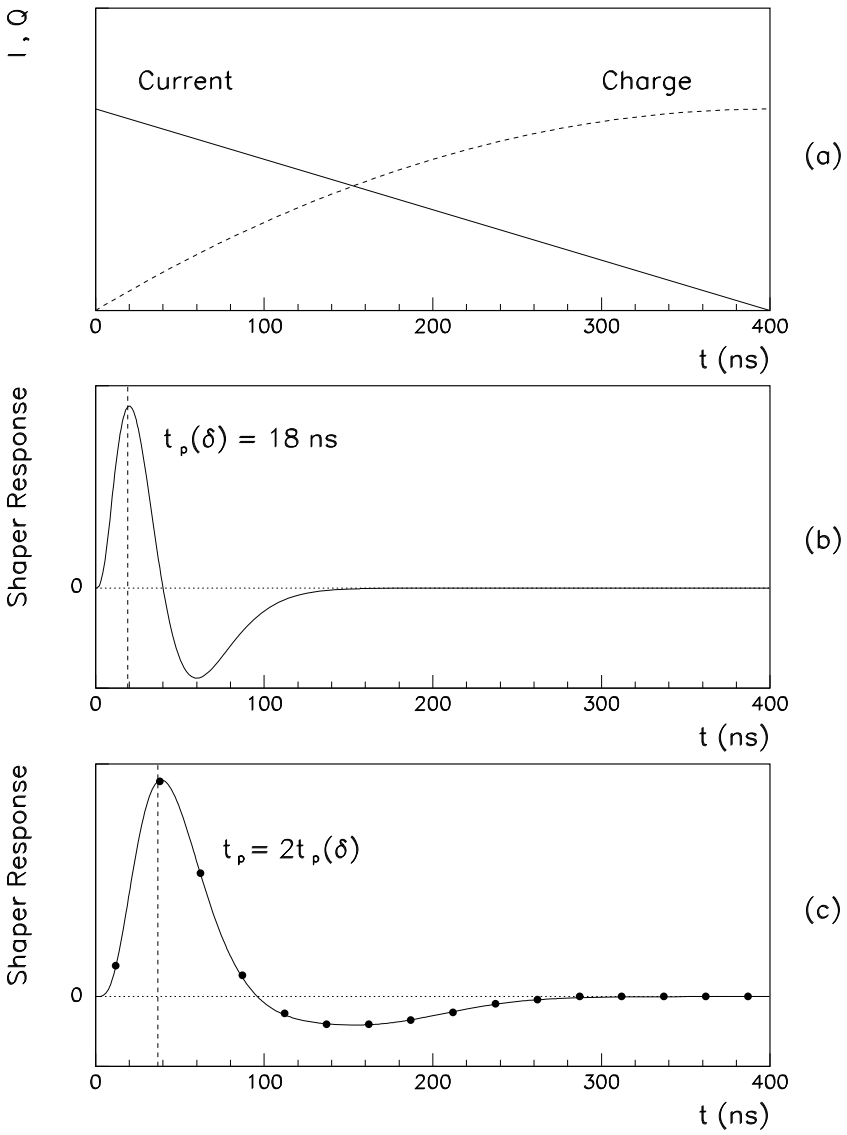

Figure 4.3: a) Ionization current and integrated charge produced by an EM shower in a calorimeter cell as a function of time. b) Shaper response to a fast (δ) pulse showing the bipolar shape with $t_p(\delta) = 18$ ns. c) Shaper response to the triangular current pulse from (a). The dots indicate the 25 ns bunch crossing interval at the LHC.

4.3 The Pointing Geometry Calorimeter Prototype

By opening up the plates with increasing depth as shown in figure 4.2, an accordion calorimeter can be made to point towards the interaction region. The barrel region of a collider calorimeter can be constructed in this way. Such a device is hermetic and is symmetric over the azimuthal angle. A two meter long "pointing geometry" accordion calorimeter prototype has been designed and built by the RD3 collaboration [35]. This prototype covered a pseudorapidity interval $0 \leq \eta \leq 1.08$ and spanned a total of 27° in azimuth with three independent modules of 9° each. The inner and outer radii of the calorimeter were 140 cm and 190 cm respectively for a total radial thickness of $25X_o$ at $\eta = 0$. This was subdivided radially into three compartments ("samplings") of thickness 9, 9 and 7 X_o to allow the shower to be sampled longitudinally. The first sampling was read out from the front of the calorimeter while the second and third samplings were read out from the back. The structure of the absorbers and readout layers for this prototype are shown in figure 4.4

A total of 73 absorber sheets were alternated with 72 layers of copper-Kapton readout electrodes and separated on either side by a LAr gap of 1.9 mm. The readout electrodes were divided laterally into five sectors in η, each with a size of $\triangle\eta = 0.216$ and read out by separate motherboards. Absorber plates and readout electrodes were bent into an accordion shape with a folding angle that increased with successive folds from 87° to 111°. The corners had a radius of curvature of 3 mm in order keep inhomogeneities in the electric field in the LAr gaps under control. The change in the folding angle with increasing radius was necessary to maintain a constant LAr gap thickness perpendicular to the plates, and therefore a constant electric field in the gaps.

The absorbers consisted of 1.8 mm thick lead sheets clad with 0.2 mm of stainless steel using a thin (100 μm) layer of prepreg. The steel cladding provided structural strength and a clean surface to the absorbers. Because the projective angle increases along the length of

the barrel, the sampling frequency decreases with decreasing $\sin\theta$, and the sampling term of the energy resolution is degraded by a factor

$$\frac{\sigma_{\text{samp}}}{E} \propto \frac{1}{\sqrt{\sin\theta}} \quad . \tag{4.3}$$

This effect can be corrected for by reducing the amount of absorber material while maintaining a constant thickness of active material. In an attempt to maintain good energy resolution at large η, the thickness of the lead absorbers was reduced to 1.2 mm for $\eta \geq 0.7$, and two additional layers of stainless steel and prepreg were added to maintain a constant sheet thickness.

Readout layers consisted of 400 μm thick triple layer printed circuit boards produced by gluing together two sheets of copper-clad Kapton. An electric field of 10 kV/cm was produced in the LAr gaps by applying a high voltage to the outer two layers of these sheets. Charge collected on the outer layers was capacitively coupled to the inner layer, which was connected to a charge sensitive preamplifier. The potential effects of shorts between the high voltage layers and the grounded absorber plates were reduced by separating regions of the electrodes using strips of resistive material.

The transverse granularity in the first two samplings was $\triangle\eta \times \triangle\phi = 0.018 \times 0.020$ where η is in rapidity units and ϕ is in radians. The granularity was reduced to $\triangle\eta \times \triangle\phi = 0.036 \times 0.020$ in the third sampling. In η this granularity was produced by etching the copper-Kapton readout electodes to produce copper pads of the correct projective size separated by narrow non-conducting strips (see figure 4.4b). To produce the desired granularity in ϕ, three adjacent electrode layers were ganged together to form a readout cell which was connected to a single preamplifier.

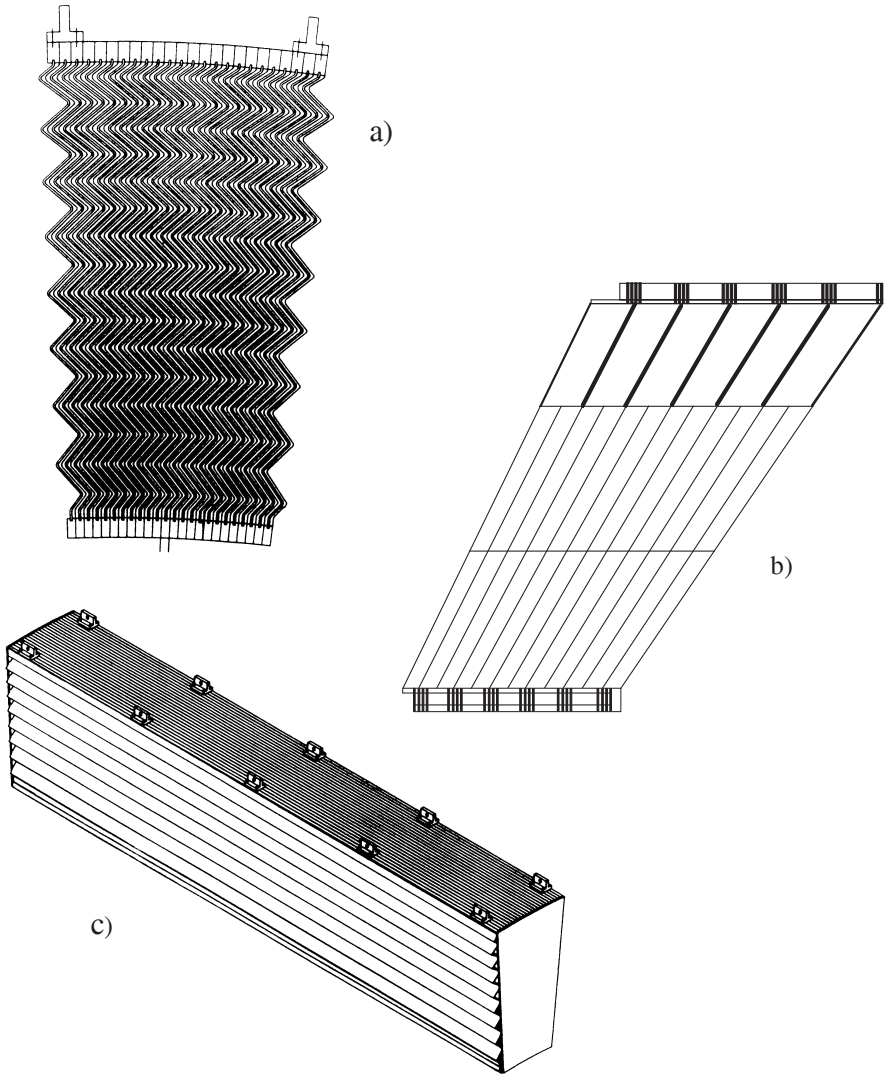

Figure 4.4: Schematic diagram of a module of the pointing geometry accordion calorimeter prototype. a) Accordion structure of the readout electrodes and absorbers. b) A readout electrode spanning one sector (12 readout cells in η) of the calorimeter and showing the segmentation in depth. Cells are formed by projective strips etched on the Kaptons. c) A fully assembled calorimeter module.

4.3.1 Electronics readout chain

Electronics channels were read out via three different systems as shown in figure 4.5. Two of these systems consisted of charge preamplifiers optimized to operate at LAr temperatures. These silicon JFETs (Si) [36] and GaAs MESFETs (GaAs) [37] were mounted on motherboards placed directly on the front and rear faces of the calorimeter inside the cryostat. A third readout system consisted of warm current preamplifiers which were connected to the calorimeter via 50 Ω cables. This scheme was referred to as "0T" because there were no transistors inside the cryostat [38]. Signals produced by the preamplifiers were shaped with $(CR)^2(RC)^3$ bipolar filters, which were designed to have an impulse peaking time $t_p(\delta)$ of 18 ns, giving a 35 ns response time to a triangular current pulse produced in the calorimeter. The shapers were followed by track and hold circuits, which could be triggered by either physics or calibration triggers. The timing was adjusted so that hold signals were generated at the peak of the shaper response. The resulting signal was then digitized using a 12-bit charge integrating ADC.

4.3.2 Calibration

Calibration of the calorimeter was achieved by the injection of shaped current pulses produced by a 12-channel current generator into the front of the electronic chain. These pulses had a fast risetime (1 ns) and an exponential decay with a time constant of about 400 ns to simulate the triangular current pulses produced by physics events. These signals were distributed to injection networks mounted on the motherboards, which injected the pulses to every fourth preamplifer on the motherboard. Adjacent channels were pulsed at different times in order to allow the crosstalk between channels to be monitored.

The calibration consisted of two parts. First, the timing of the track and hold gate signal was optimized with respect to the shaper signal. This was accomplished by injecting

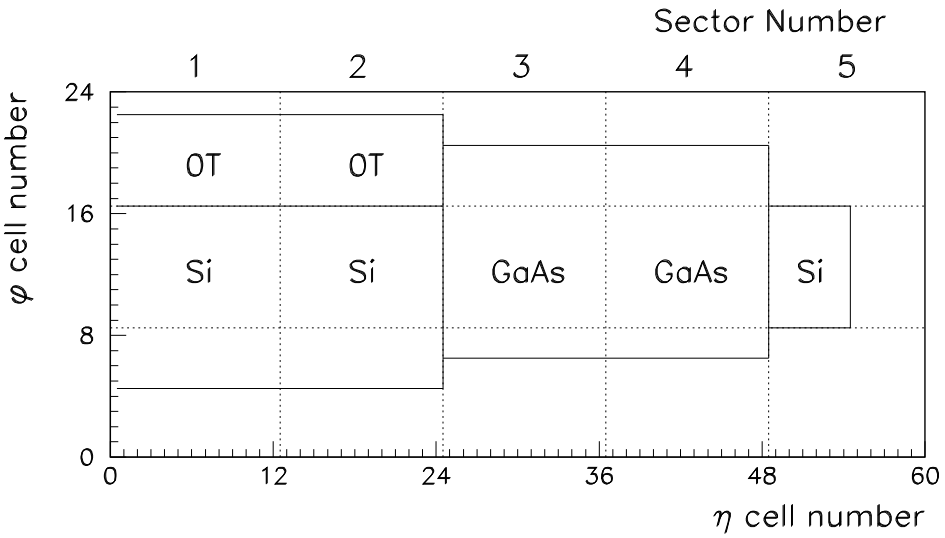

Figure 4.5: Regions of the calorimeter equipped with Si, GaAs and 0T preamplifiers. Solid lines separate regions with different electronics. Regions not labeled were not equipped during this test period. Dashed lines indicate boundaries between η sectors and ϕ modules. Each of the three ϕ modules is eight cells wide and spans all five sectors in η. The individual sectors are 12 cells wide in η.

calibration pulses into the electronics chain while the timing of the track and hold gate was adjusted in 1.5 ns increments over a 60 ns range using a computer controlled delay. A quadratic interpolation around the region of maximum response was used to determine the peaking time. Next, the calibration pulses were timed with respect to actual physics triggers in order to optimize the track and hold response to physics signals.

The second stage of the calibration procedure was the determination of ADC gain coefficients which allowed the conversion between ADC counts and the corresponding charge detected. The ADC response to a series of calibration pulses of various known amplitudes was measured for each electronic channel, and the results were fitted with a third-order polynomial.

Chapter 5

Electron Energy Resolution

5.1 Experimental Setup

Tests of the pointing geometry accordion prototype were performed in the H8 beam line in the North Area at the CERN SPS. Secondary and tertiary electron and pion beams in an energy range of 10 to 287 GeV were available. The momentum spread of the beam was estimated to be $\delta P/P \leq 0.3\%$ for the secondary beam, and $\delta P/P \leq 0.7\%$ for the lower energy tertiary beam [9]. The beam magnets were adjusted to provide a beam spot size that approximately covered one calorimeter cell ($\sim 3 \times 3$ cm^2). The experimental setup is illustrated in figure 5.1. The EM calorimeter prototype was installed in a purpose built cryostat, which consisted of a 1.2 mm thick aluminium outer wall followed by 30 cm of low density foam and an 8 mm stainless steel inner wall. Including cables, mechanical supports and inactive LAr between the calorimeter and the cryostat inner wall, the total amount of passive material in front of the calorimeter was estimated to be $\sim 1\, X_0$ at $\eta = 0$, increasing as $1/\sin\theta$ along the length of the barrel [35]. The EM calorimeter was backed up by an accordion geometry hadronic calorimeter prototype which was also developed by the RD3 collaboration [12]. The cryostat could be rotated about two axes in such a way that the

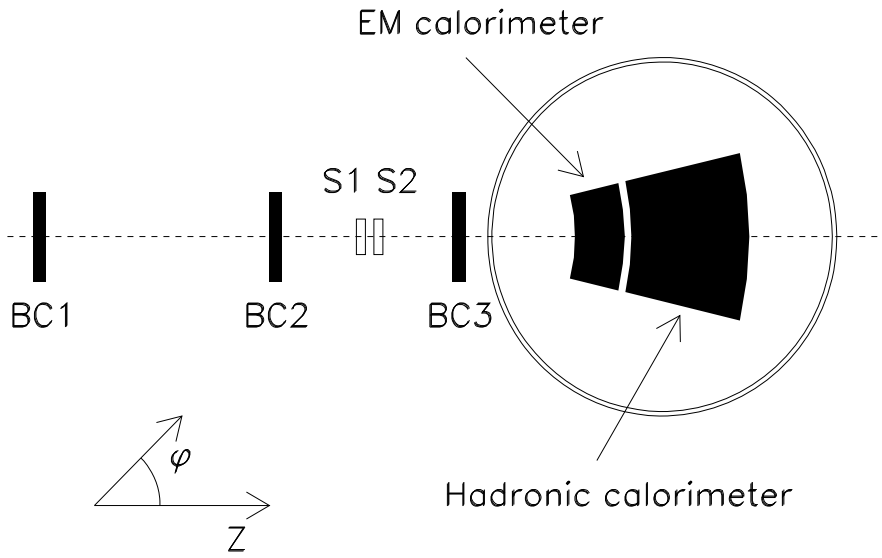

Figure 5.1: Schematic diagram of the RD3 beam test apparatus. The beam was oriented along the z axis. The three beam chambers BC1, BC2 and BC3 were placed in the beam line in front of the cryostat and separated by several metres. Triggering was provided by the scintillators S1 and S2. The pointing geometry EM calorimeter prototype was installed in a purpose built cryostat with a radius of $\sim$ 1.5 m, and was backed up by an hadronic calorimeter prototype. The figure is not shown to scale.

beam would strike the calorimeter face at the same projective angle as would a particle produced at the interaction point of the ATLAS detector at the LHC.

First level triggering was accomplished by means of two $3 \times 3\,\mathrm{cm}^2$ scintillators located in front of the cryostat. Three proportional wire chambers were used to provide electron impact positions on the calorimeter face. A second level trigger selected clean electron events using information from the wire chambers. When an event was selected, ADC output values of all electronics channels were written to magnetic tape. Data acquisition was controlled by a Unix workstation which provided online monitoring of the calorimeter, wire chambers and scintillators, controlled the position of the cryostat and allowed various types of data runs to be selected and initiated.

5.2 The Electron Sample and Event Reconstruction

Data were collected during beam test periods in the spring and fall of 1993. Data runs typically lasted about 10 minutes, during which time about 5000 events were recorded. Large area scans were performed with 197.5 GeV and 287 GeV electron beams. These scans each consisted of about 100 individual data runs taken in different calorimeter cells spread over sectors 1 to 4 ($0 \leq \eta \leq 0.86$). In addition, data were collected using 10, 20 and 30 GeV electron beams in two cells in the Si region. Calibration runs were performed periodically in order to determine ADC pedestal and gain values. These values were recorded in a database for use in offline analysis.

Offline analysis was performed using RD3 analysis software run on an IBM 3270 at CERN (CERNVM). This software was used to select clean events, to provide shower position information and to reconstruct energy clusters. Events were read from magnetic tape and reconstructed as follows. ADC pedestal and gain values corresponding to the selected run were read from a database. The energy deposited in each calorimeter cell was calculated by subtracting the pedestal from the raw ADC value for that event, and substituting this new ADC value into a third order polynomial function of the gain coefficients. The energy of the incident electron was determined by summing the energy in each sampling of a 3×3 cluster of cells surrounding the cell possessing the most energy. The absolute energy scale was fixed by setting the mean value of the electron energy spectrum equal to the beam energy at 287 GeV. The position of the shower centroid in each sampling was found by computing the energy-weighted barycentre of the cluster. An independent position measurement was made by extrapolating the line connecting the hits in each of the three wire chambers to the calorimeter face. Data summary files produced by this preliminary analysis were transferred to a cluster of Hewlett-Packard workstations at the University of Victoria where a more detailed analysis was performed.

Figure 5.2a shows the energy spectrum of the events recorded for a typical data run at an electron beam energy of 197.5 GeV. The plot shows a narrow peak near 200 GeV produced by electron events. The peak centred near zero energy was produced by minimum ionizing signals from $\sim$ 200 GeV muons which also survived the beam momentum selection. The low broad peak between $\sim$ 10 GeV and $\sim$ 160 GeV was the result of pion contamination in the beam, and could be effectively removed by selecting events within an energy window of 170 to 220 GeV centred around the electron peak [39]. To remove any remaining hadron contamination, selection criteria were applied to the energy deposited in the hadronic calorimeter. The longitudinal profile of hadronic showers is characterized by the *interaction length*, which is much longer than the radiation length which characterizes EM showers. EM showers were almost completely ($> 95\%$) contained within the EM calorimeter whereas at high energies a significant fraction of the hadronic shower energy was deposited beyond the EM calorimeter in the hadronic calorimeter [16]. Therefore, selecting events with low energy deposition in the hadronic calorimeter favoured electrons over pions. The remaining low energy tail was attributed to electrons which had been degraded in energy by material upstream of the calorimeter [8, 35]. Selection cuts were also applied to the beam chamber position information in order to select events which had a correctly reconstructed impact position (see section 5.5.1). The events from figure 5.2a which survived all the above selection cuts are plotted in figure 5.2b. A similar procedure was used to select clean events for runs at 10, 20, 30 and 287 GeV. The data samples which were produced in this manner are referred to as *electron samples*.

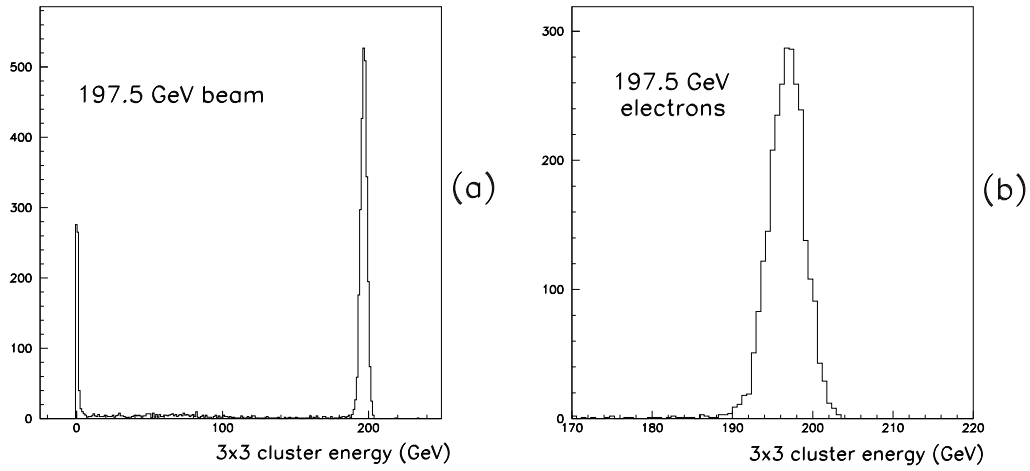

Figure 5.2: Energy spectrum measured by the EM calorimeter during a typical 197.5 GeV data run. The events which survive selection cuts are shown in the figure on the right.

5.3 Uncorrected Energy Resolution

The energy resolution is given by the ratio of the peak width (σ) to the mean energy (μ) of the electron sample. The width and the mean of the electron peak were determined by performing a maximum likelihood fit of a Gaussian distribution to the region surrounding the peak but excluding the non-Gaussian low energy tail (see section 5.2). A contribution to the width of 0.7% (0.3% for $E > 30$ GeV) due to the momentum spread of the beam particles was quadratically unfolded from σ/μ to give the uncorrected energy resolution of the calorimeter. The uncorrected resolution was determined at each available electron beam energy using data from the Si sector 1 region. At 10, 20 and 30 GeV the uncorrected resolution was measured using $\sim$ 3 runs at each energy taken in a single cell. Data from several different cells were combined in order to obtain average values for the resolution at 197.5 GeV and 287 GeV. To isolate the intrinsic energy resolution performance, response variations between cells were eliminated by individually normalizing the mean response in

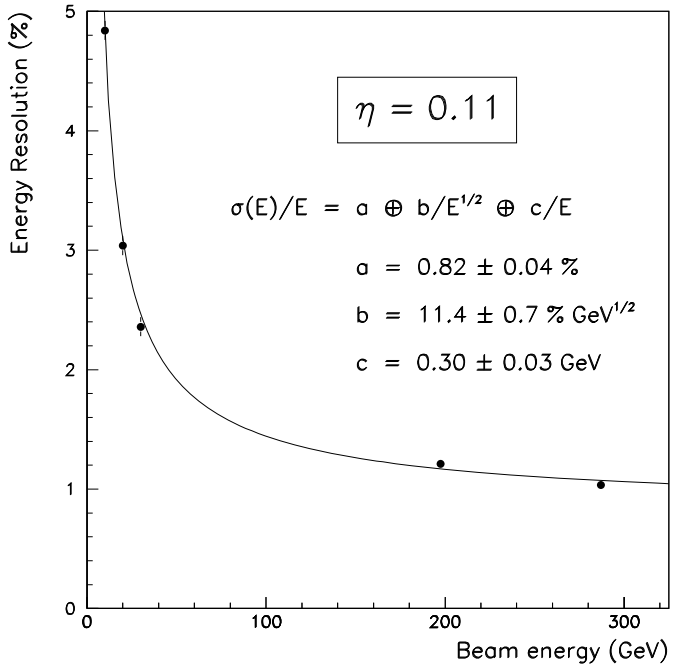

Figure 5.3: Uncorrected energy resolution as a function of the electron beam energy. Uncertainties in the data points are shown, or are smaller than the dots. The solid line represents the best fit to the data and the values of the parameters a, b and c are listed. E is in GeV.

each cell to one (see also section 5.7). This was verified by comparing the average value of the resolutions obtained for the individual runs with the resolution obtained when all of the individually normalized runs were combined. The two values were found to be the same within statistical errors. The uncorrected energy resolution is plotted as a function of the incident beam energy in figure 5.3. A fit with equation 2.4 yielded

$$\frac{\sigma(E)}{E} = (0.82 \pm 0.04)\% \oplus \frac{(11.4 \pm 0.7)\%}{\sqrt{E}} \oplus \frac{(0.30 \pm 0.03)}{E} \quad , \tag{5.1}$$

where E is in GeV.

5.4 Cluster Weighting Corrections

Segmentation of the calorimeter in depth permitted the shower to be sampled at three different depths longitudinally. The total energy of the shower was reconstructed by a weighted sum of the energy measured by a 3×3 cluster of cells in each sampling. The general form of the weighted sum used is

$$E = \alpha(E_1 + \beta(E_2 + \gamma E_3)) \quad , \tag{5.2}$$

where E is the reconstructed shower energy, E_i is the energy measured in the i_{th} sampling, and α, β, γ are weighting factors. In this parameterization β and γ are free parameters and α is chosen so that the mean value of E is equal to the mean energy of the uncorrected sample as described in section 5.3. Because the energy resolution is given by the ratio of the peak width to the mean energy, it is independent of the value of α.

There are several physical reasons why β and γ are not necessarily equal to unity. Charge deposited in the first sampling is transferred to preamplifers at the front face of the calorimeter, while signals from the second and third samplings are read out from the back. Narrow copper lines carry the signal from the middle sampling to the rear surface of the calorimeter. A small fraction of the ionization charge produced in the third sampling will therefore be collected on these lines and contribute to the signal in the second sampling. The proximity of these lines to the electrodes is also known to produce crosstalk between the second and third samplings [35]. Furthermore, the pointing accordion geometry causes a small variation with depth of the sampling frequency and of the electric field configuration near bends in the plates. Because the longitudinal shower profile is dependent on the incident particle energy, the parameters of equation 5.2 may also be energy dependent.

The resolution was optimized with respect to the parameters β and γ by fitting Gaussian functions to the energy reconstructed using equation 5.2. The energy resolution was expected to be more sensitive to the value of β than to γ because a larger fraction of the

total energy was deposited in the second sampling than in the third. Furthermore, β was presumed to have a value close to unity and to be less dependent on the beam energy. For these reasons an energy independent value for β was sought. The obvious choice $\beta = 1.0$ did not produce the best possible resolution at low energies, however $\beta = 0.93$ was found to be consistent with the optimum resolution at all available energies.

The optimum value for γ was estimated at each available beam energy by plotting the energy resolution as a function of γ with β fixed to 0.93. This is illustrated in figure 5.4 for 197.5 GeV electrons. The uncertainty in γ was taken to be the estimated variation in γ which degraded the resolution by an amount equal to the average uncertainty in the resolution. The measured energy resolution had an uncertainty of typically 0.5% independent of the beam energy, however the sensitivity of the resolution to the value of β decreased with the beam energy, resulting in large uncertainties at low energies. This was expected because the energy resolution at low energies is dominated by electronics noise, while cluster weighting corrects for effects contributing to the constant and sampling terms of the energy resolution.

At energies above 10 GeV γ was found to be consistent with 1.0, while at 10 GeV it was consistent with zero, as is shown in figure 5.5a. This can be understood by noting that the mean energy measured in the third sampling at this beam energy is only slightly above the level at which noise contributes to the signal. The electronics noise in cells equipped with Si MESFETs had previously be found to produce incoherent noise at the level of $\sim$ 50 MeV in the first and second samplings, and $\sim$ 70 MeV in the third sampling [35]. The total incoherent noise in the third sampling was therefore expected to be $\sim$ 210 MeV, given by the quadratic sum of the noise in the nine cells in the energy cluster. The mean energy measured in the third sampling is plotted as a function of the beam energy in Figure 5.5b, where the error bars indicate the rms of energy distribution. From this figure it is clear that electronics noise is the dominant contribution to the measured signal, and so setting γ to zero at low energies can improve the energy resolution.

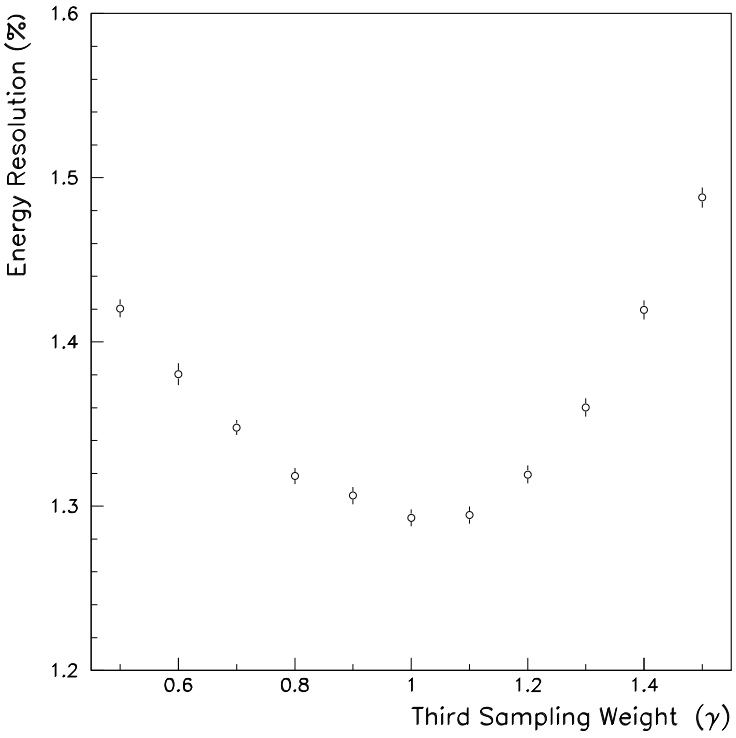

Figure 5.4: Energy resolution as a function of the third sampling weight γ for 197.5 GeV electrons. The value of β was fixed to 0.93.

The reconstructed energy was then conveniently parameterized by

$$E = \alpha(E_1 + 0.93 \cdot (E_2 + \gamma E_3)) \quad \text{where} \quad \gamma = \begin{cases} 0 & \text{if } E \leq 10 \text{ GeV} \\ 1 & \text{if } E > 10 \text{ GeV} \end{cases} \quad . \tag{5.3}$$

The term *reconstructed energy* will be used from here on to refer to the weighted sum of a 3×3 energy cluster in each sampling computed using equation 5.3. The energy resolutions obtained at each beam energy using the reconstructed energies were fitted to equation 2.4 and the results are listed in table 5.1. The sampling and constant terms are seen to improve relative to the uncorrected resolution measured in section 5.3.

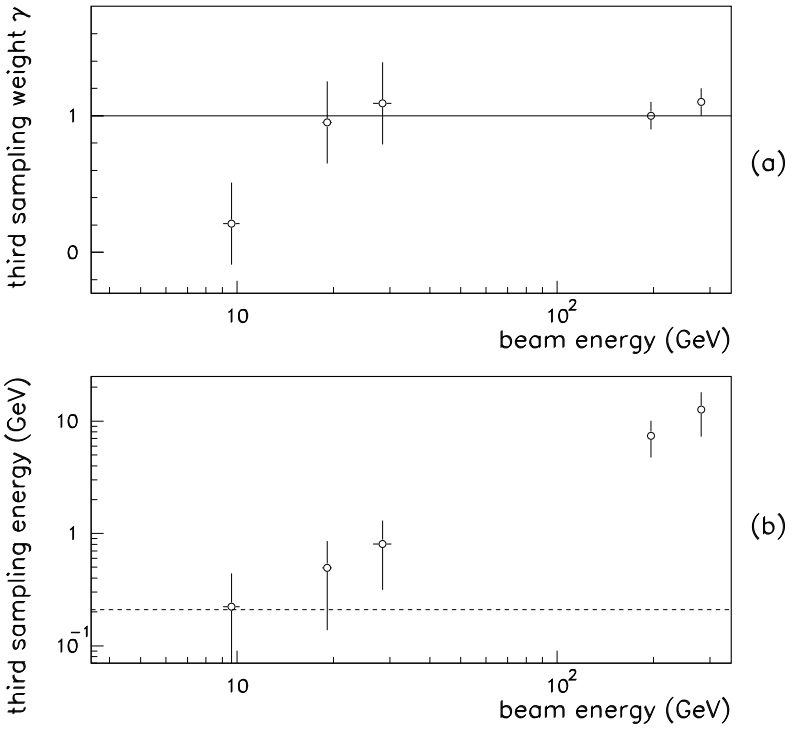

Figure 5.5: a) Estimated optimum value of the third sampling weight γ as a function of the particle energy. b) Energy deposited in the third sampling as a function of the reconstructed particle energy. The dashed line represents the rms of the electronics noise in the cluster.

	$a(\%)$	b (% GeV $^{1/2}$)	c (GeV)
uncorrected	0.82 ± 0.04	11.4 ± 0.7	0.30 ± 0.03
cluster weighted	0.66 ± 0.05	10.5 ± 0.7	0.31 ± 0.03

Table 5.1: Comparison of the energy resolution fitting parameters a, b and c obtained with and without applying cluster weighting corrections to the electron data sample.

5.5 Position Dependent Corrections

5.5.1 Impact point reconstruction

Two independent methods were available for determining particle impact positions on the calorimeter face. Electron impact positions could be found by extrapolating the positions measured by the three wire chambers to the front face of the calorimeter. Positions reconstructed in this way are referred to as *beam chamber positions*. This system required an accurate knowledge of the location of the cryostat, of the prototype within the cryostat and of the wire chambers in order to correctly map impact points onto the calorimeter face. Effects such as material shrinkage at cryogenic temperatures contribute to the uncertainty in these positions. As a result, the locations of cell edges and the exact size of calorimeter cells were not precisely known with respect to this coordinate system. These had to be determined by examining the calorimeter response to electron events (see section 5.5.2), introducing additional uncertainty to the beam chamber position measurements.

Cluster positions were determined by computing the energy weighted barycentre of a 3×3 cluster of cells in the first sampling of the calorimeter. Clustering effects tended to reconstruct impact points away from the cell edges in both η and ϕ, producing a small gap in the position spectrum at cell edges. The η cluster position consistently biased reconstructed impact points towards the centre of the cell, resulting in an S-shaped curve when plotted against the beam chamber position as shown in figure 5.6a. The cluster position in the ϕ direction was linear with respect to the beam chamber position (figure 5.6b). The η and ϕ positions are expressed in *cell units* in which the cell size is normalized to one and the cell centres are at integer values. Because calorimeter reconstructed cluster positions were directly tied to the calorimeter, they were not susceptible to the imperfections of the beam chamber position reconstruction. The size of the calorimeter cells and the location of cell edges were known precisely with respect to the cluster position coordinate system.

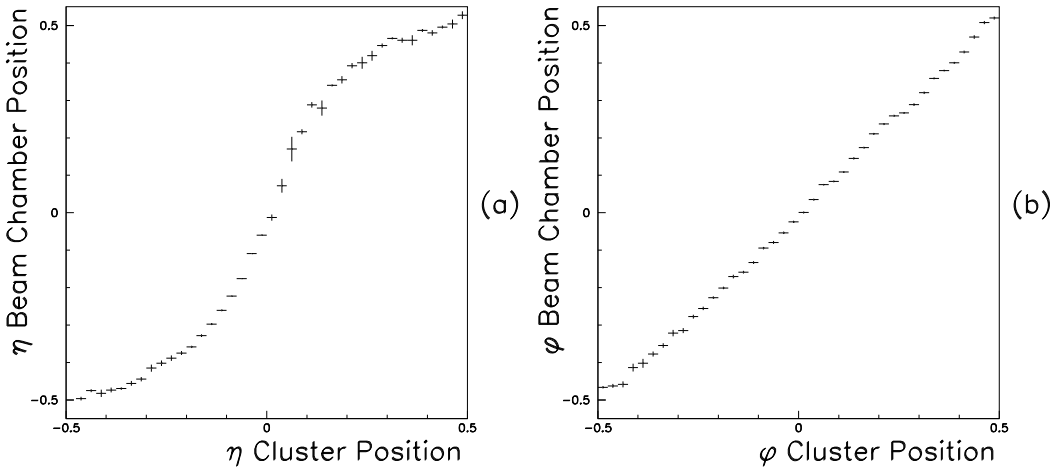

Figure 5.6: Reconstructed beam chamber position as a function of the (3×3) cluster position (a) in η and (b) in ϕ.

Comparisons between the beam chamber positions and the cluster positions reconstructed for different data runs indicated that there were systematic offsets in the beam chamber positions between runs. These were attributed to the encoders which provided the location of the cryostat. Plots of the calorimeter energy response as a function of the beam chamber η position (see section 5.5.2) were found to have a smaller rms than similar plots using cluster positions. This was attributed to the fact that the decrease of the response near the cell edges was partially washed out by the uncertainty in the beam chamber position. Because the cluster position tends to bias impact points towards the cell centre, the position scale near the cell edges is effectively stretched so that the position resolution improves near the cell edges. This is due to increased energy sharing between cells in the nonet when an electron strikes the calorimeter near cell edges [39]. Position dependent energy corrections (section 5.5.3) were found to be more effective at improving the calorimeter energy resolution when cluster positions were used. Therefore, only cluster positions were retained.

5.5.2 Position dependent response variations

The position dependence of the energy response was determined by plotting the average reconstructed energy as a function of the impact point in η and ϕ as given by the cluster position. Because the amplitude of the position dependent response was somewhat smaller than the energy resolution of the calorimeter, it was necessary to combine electron data from runs in several different cells in order to obtain sufficiently good statistics to determine the shape of the η and ϕ response with a reasonable degree of precision. Approximately 50 000 events distributed over eighteen different cells in the Si sector 1 region were used to determine the calorimeter response to 197.5 GeV electrons. At 287 GeV, about 20 000 events in ten cells in the same region were used. The energy response of the accordion calorimeter was found to be dependent on the impact position of the incident particle within a cell at the $\sim 1\%$ level in both the η and ϕ directions. The normalized calorimeter response to high energy electrons is plotted as a function of the η and ϕ positions in figure 5.7.

In the η direction the accordion calorimeter is geometrically equivalent to a parallel plate calorimeter, so the variation in the response is not due to geometrical effects, but to the clustering used to reconstruct the particle energy. A particle striking the calorimeter near the centre of a cell deposits most of its energy within a 3×3 cluster of cells surrounding the hit cell. The shower produced by a particle striking near the edge of a cell is not as well contained within this cluster and so the calorimeter response will decrease near cell edges. The response variation caused by this effect was measured using 197.5 GeV electron data to have an rms of $0.69\% \pm 0.03 \pm 0.01\%$ (see table 5.2). This effect could be reduced by reconstructing the shower energy using 5×5 clusters of cells in order to reduce the energy leakage, however 3×3 energy clusters are preferable because they introduce less electronics noise.

The response variation in the ϕ direction is a combination of the clustering effect

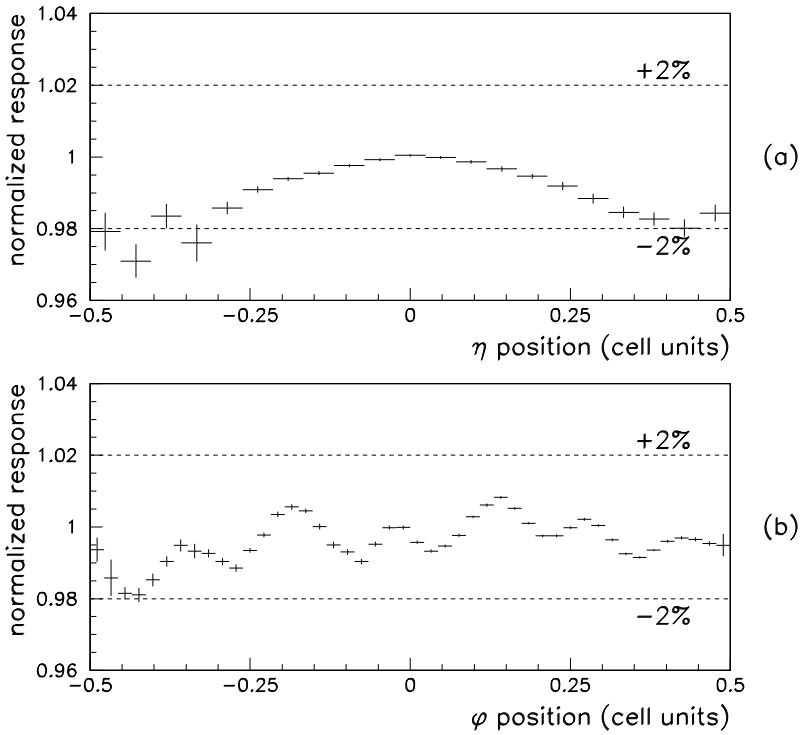

Figure 5.7: Normalized calorimeter response as a function of the electron impact point in η (a) and in ϕ (b). The statistical error on the average response in each bin is shown.

discussed above and geometrical effects related to the accordion structure. The origin of the geometrical effects can be understood by considering a hypothetical non-interacting particle passing though the calorimeter. The thickness of LAr traversed by such a particle varies with an rms of $\sim 2\%$ depending on the impact point within a cell [40]. This effect is reduced in the case of real particles by the transverse spread of the EM shower. However, the calorimeter response is enhanced when a particle is incident in a region of a cell where the average thickness of LAr traversed by particles in the shower is more than the average thickness over the entire cell. The three-fold structure resulting from the ganging of readout layers to form a readout cell is reproduced by the ϕ response. The rms of the response

modulation in ϕ was measured using 197.5 GeV electrons to be $0.61\% \pm 0.03 \pm 0.05\%$ and was approximately energy independent.

5.5.3 Response corrections

Position dependent response non-uniformities contribute directly to the constant term of the calorimeter energy resolution. It is therefore desirable to correct these effects to the highest degree that is practical, particularily at high energies where the constant term dominates. In the work described here, position dependent corrections were applied to 197.5 GeV and 287 GeV electron data only, because at lower beam energies they were found to have no significant effect on the calorimeter energy resolution. Position dependent corrections can be applied either globally, in which case the same correction is applied to all cells in the calorimeter, or locally, where each cell is individually corrected with cell specific corrections. Because local corrections require high statistics in each cell, their effectiveness is difficult to evaluate. Only global corrections are retained in this work.

The procedure for applying and evaluating the effectiveness of position dependent corrections is as follows. The response was plotted as a function of each of the two coordinates η and ϕ as measured by the cluster position. The response variations with respect to the two coordinates are independent, so the mean energy response $R(\phi, \eta)$ is separable into functions of η and ϕ (see for example figure 5.7):

$$R(\eta, \phi) = F(\phi)\ G(\eta)\ . \tag{5.4}$$

These curves were then fitted with the functions $f(\phi)$ and $g(\eta)$, which approximated the true response $F(\phi)$ and $G(\eta)$. The electron data sample was then corrected on an event by event basis by dividing the reconstructed energy of each event by the normalized response function $r(\phi, \eta) = f(\phi)g(\eta)$. Because the function $r(\phi, \eta)$ is an approximation to the true response $R(\phi, \eta)$ there will in general be some residual position dependence.

	rms (%)	Corrected rms (%)
η response at 197.5 GeV	$0.69 \pm 0.03 \pm 0.01$	$0.31 \pm 0.04 \pm 0.01$
η response at 287 GeV	$0.83 \pm 0.07 \pm 0.01$	$0.35 \pm 0.09 \pm 0.01$
Energy specific correction	–	$0.35 \pm 0.09 \pm 0.01$
ϕ response at 197.5 GeV	$0.61 \pm 0.03 \pm 0.05$	$0.21 \pm 0.4 \pm 0.05$
Corrected with $f_1(\phi)$	–	$0.43 \pm 0.3 \pm 0.05$
ϕ response at 287 GeV	$0.50 \pm 0.2 \pm 0.05$	$0.30 \pm 0.2 \pm 0.05$
Energy specific correction	–	$0.17 \pm 0.03 \pm 0.05$

Table 5.2: Values of the rms of the response variation in η and ϕ before and after position dependent corrections were applied. The statistical and systematic uncertainties are also listed. All corrections were made using $g(\eta)$ and $f_2(\phi)$ fitted to the response determined for the 197.5 GeV electron sample except where otherwise noted. "Energy specific corrections" utilize response functions which were fitted to data at 287 GeV.

The effectiveness of the position corrections was evaluated by comparing the energy resolution of the electron sample before and after corrections were applied. This gave a direct measure of the improvement resulting from the correction, however it only describes the true resolution of the calorimeter if the electron samples were uniformly distributed over each cell, which was not the case. Since data were collected with the beam pointed directly at the middle of each cell, fewer events were recorded near cell edges where response non-uniformities were the greatest. The rms of the residual corrected response variation gives an indirect measure of the improvement in the resolution which is less subject to biasing. The corrected response was plotted as a function of each of the two position coordinates and the rms of the residual modulation was evaluated over one cell. The improvement in the resolution that can be expected by applying these corrections to a data sample uniformly distributed over a cell is given by the quadratic sum of the difference in the uncorrected and corrected rms values in η and ϕ. Poor statistics near cell edges increase the uncertainty of these measurements but do not bias the result. The values of the rms of the position dependent response variation and their residuals after correction are listed in table 5.2.

Systematic uncertainties in the position dependent response were estimated by com-

paring the cell to cell variations in the measured position dependent response before and after position dependent corrections were applied. The 197.5 GeV electron data sample was divided into two statistically independent samples on a cell by cell basis. Each sample was separately used to determine the response variation in η and ϕ. The systematic error in the rms of the position dependent response was determined by comparing the response curves for the two data samples. The η dependent response variation was found to show very little sensitivity to cell to cell response variations. This was to be expected since the η dependence of the response was attributed to clustering effects, and not to the mechanical structure of the calorimeter. The systematic error in the measurement of the η dependent response was estimated to be on the order of 0.01% and was attributed to calibration errors in cells in the (3×3) energy clusters. The cell to cell variation in the ϕ dependent response was found to be much larger due to mechanical imperfections in the accordion structure of the cell. The uncertainty in the rms due to these effects was estimated to be 0.05%, and does not include differences in the response due to variations in the experimental setup between the two beam test periods, such as slight differences between angles of incidence of the electron beam on the calorimeter face. Because the 197.5 GeV and 287 GeV electron samples were collected during two different beam test periods, it is likely that the difference between the values of the rms of the ϕ dependent response measured at these two energies is entirely attributable to systematic effects rather than to an energy dependence of the response variation.

The normalized response in the η direction was fitted with the function

$$g(\eta) = P_1 + P_2 \sin(\pi\eta + \pi/2) \quad , \tag{5.5}$$

where η is in cell units and P_1 and P_2 are the fitting parameters. Figure 5.8 shows the η dependence of the response before and after applying this correction to 197.5 GeV data. The residual rms of $0.31\% \pm 0.04 \pm 0.1\%$ was attributed to imperfections in the fit at the cell edges, and to the anomally at $\eta \approx 0.1$ which was a consequence of the beam profile at this energy. η corrections applied to 287 GeV data were also found to correct the rms to

the $\sim 0.3\%$ level independent of whether the fitting parameters were obtained using 197.5 GeV data or 287 GeV data (see table 5.2). The residual rms was largely attributable to statistical variations in the response, due to low event statistics in some regions of the cell. The effectiveness of this simple correction at reducing the rms of the η dependence of the response, independent of the beam energy and beam test setup, combined with the small value of the cell to cell variation in the η dependence, suggest that the it should be possible to correct the η dependent response to a high degree in an experiment such as ATLAS. In the present case, measurements of the effectiveness of η corrections are statistically limited. A uniform beam profile over an area of at least an entire cell during data taking would allow a more precise determination of the η dependent response.

Two different functions were used to fit the response in the ϕ direction. Initially a simple three parameter response function was used. This function was similar to that used in [35]:

$$f_1(\phi) = 1.0 + P_1 x^2 + P_2 \sin(6\pi\phi - \pi/2) + P_3 \sin(12\pi\phi + \pi) \quad . \tag{5.6}$$

The decrease in response near cell edges due to the clustering effect is corrected by the quadratic term, and the remaining two terms describe the threefold structure of the calorimeter cells. This function was found to reproduce the basic shape of the ϕ response, but did not describe the response well. Corrections applied to 197.5 GeV electron data produced a residual ϕ dependence with an rms of $0.43\% \pm 0.04 \pm 0.05\%$. This residual was largely attributable to the inadequacy of the response function rather than to statistical fluctuations, suggesting a need for a more specialized correction function. A second ϕ response correction function was obtained by using harmonics of $\sin(\pi\phi)$ and allowing the phases to vary freely. The resulting eight parameter function

$$f_2(\phi) = P_1 + P_2 \sin(\pi\phi + \pi/2) + P_3 \sin(2\pi\phi + P_4) + P_5 \sin(6\pi\phi + P_6) + P_7 \sin(13\pi\phi + P_8) \tag{5.7}$$

was found to describe the data very well. This function is shown in figure 5.9 fitted to the response curve obtained for 197.5 GeV electrons. The residual ϕ modulation after the correction was applied is also shown in this figure, and was found to have an rms of

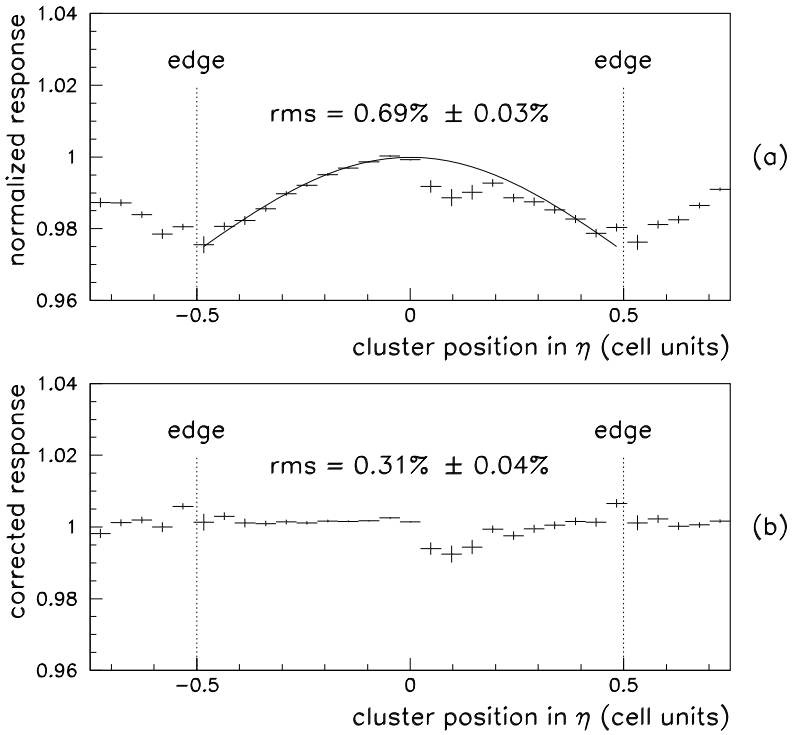

Figure 5.8: (a) The normalized response variation in η fitted with a correction function. (b) The response in η after the correction is applied.

$0.21\% \pm 0.04 \pm 0.05\%$. Comparison of the residual ϕ modulation obtained when 197.5 GeV and 287 GeV data were separately fitted with $f_2(\phi)$ indicates that this correction was equally effective at both energies. However, when the 287 GeV electron sample was corrected using the same function fitted to 197.5 GeV data, the residual rms was seen to worsen to $\sim 0.3\%$. This effect is probably due to differences in the calorimeter alignment between beam test periods (see section 5.5.2) and cell to cell response variations, rather than indicating an energy dependence of the ϕ response. Reducing the rms of the residual response variation in ϕ direction to the level of $\sim 0.3\%$ has been shown to be relatively straightforward, however reducing it much beyond this level will clearly require more sophisticated corrections.

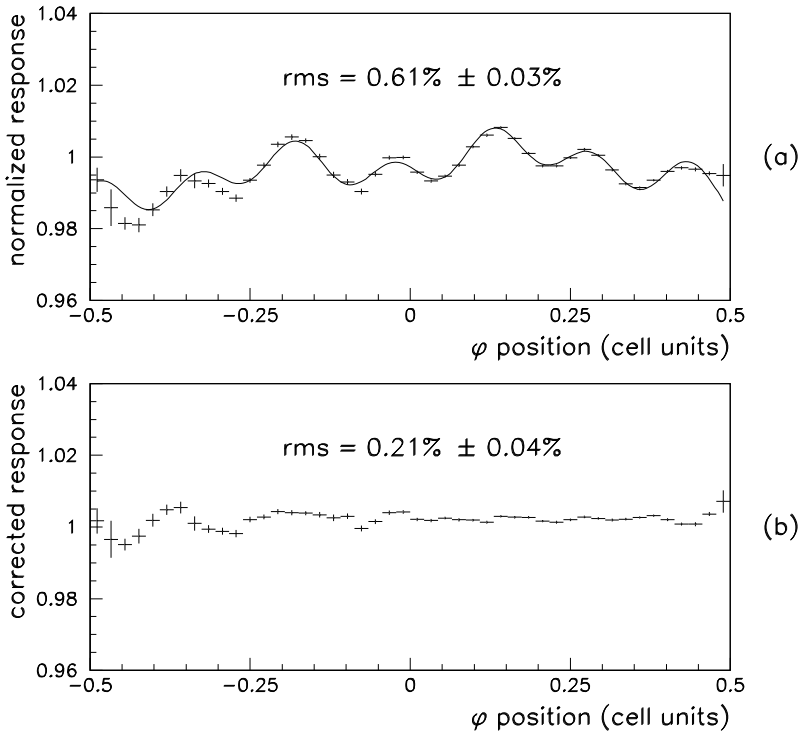

Figure 5.9: (a) The normalized response variation in ϕ fitted with an eight parameter correction function. (b) The response in ϕ after the correction is applied.

5.6 Corrected Energy Resolution

The corrected electron energy resolution of the prototype was determined by applying cluster weighting and position dependent corrections to the electron samples. The resolution at 197.5 GeV and 287 GeV was determined by combining data from several cells. The mean reconstructed energy was normalized to one in each cell in order to correct for cell to cell response non-uniformities as discussed in section 5.3. Cluster weighting corrections were applied at all energies using the optimum weighting parameter values determined in

section 5.4. Position dependent energy corrections were applied only to 197.5 GeV and 287 GeV electron data and used energy specific ϕ corrections. At lower energies where the resolution is dominated by electronics noise, position dependent corrections were found to have no significant effect and so were not used.

Systematic errors in the measured energy resolution were estimated in a manner similar to that used for the rms measurements (section 5.5.3). The 197.5 GeV electron sample was separated into two independent samples and the position dependence of the response was determined for each sample. To evaluate the effect of correlations introduced by correcting a data sample with fitting functions obtained using the same data sample, the two samples were independently fitted with position dependent correction functions. The parameters obtained by fitting one sample with the functions $f_2(\phi)$ and $g(\eta)$ were used to correct the response of the other sample. The energy resolution obtained in this way was compared with the resolution measured when each sample was corrected using fitting functions determined on the same sample. The sensitivity of the energy resolution as to which data sample the response functions were originally fitted was found to be small. The cell to cell variation in the energy resolution was found to be significantly larger than the statistical uncertainty in the resolution measurements. The source of these variations in energy resolution was believed to be cell to cell variations in the ϕ dependence of the response as discussed previously. A systematic uncertainty of $\pm 0.02\%$ was estimated for the energy resolution measured at 197.5 GeV and 287 GeV. At lower energies where only a few data runs were available at each energy, the uncertainties were estimated using the variance of the measured resolutions.

The corrected energy resolutions are shown in table 5.3 and are plotted as a function of the beam energy in figure 5.10. It can be seen that each of the cluster weighting corrections, η corrections and ϕ corrections independently applied to the data samples produce an improvement in the energy resolution at all beam energies, and that the cluster weighting correction has the most significant effect. The energy dependence of the resolution was

Beam Energy	10 GeV	20 GeV	30 GeV	197.5 GeV	287 GeV
Uncorrected	4.84 ± 0.05	3.04 ± 0.03	2.36 ± 0.04	1.21 ± 0.005	1.03 ± 0.01
Cell weighted	4.59 ± 0.05	2.93 ± 0.03	2.28 ± 0.04	0.998 ± 0.004	0.918 ± 0.008
Eta corrected	-	-	-	1.16 ± 0.004	0.994 ± 0.008
Phi corrected	-	-	-	1.07 ± 0.004	0.988 ± 0.008
All corrections	4.59 ± 0.05	2.93 ± 0.03	2.28 ± 0.04	0.808 ± 0.004	0.761 ± 0.008
Systematic error	± 0.07	± 0.07	± 0.07	± 0.02	± 0.02

Table 5.3: Measured energy resolution (in %) at various beam energies before and after corrections were applied. The estimated systematic and statistical errors are also listed.

	$a(\%)$	b (% GeV $^{1/2}$)	c (GeV)
uncorrected	0.82 ± 0.04	11.4 ± 0.7	0.30 ± 0.03
corrected	0.40 ± 0.07	10.2 ± 0.6	0.33 ± 0.02
reference [35]	0.35 ± 0.04	9.99 ± 0.29	0.2823 ± 0.017

Table 5.4: Energy resolution fitting parameters obtained before and after η, ϕ and cluster weighting corrections were applied. The values reported by in [35], which were obtained using the same prototype but different data samples, are listed for comparison.

determined by fitting equation 2.4 to the resolution measured at the five available beam energies. Table 5.4 lists the values of the parameters a, b and c which were obtained for the uncorrected and corrected energy resolution. The results reported in [35] which were obtained for the same prototype during a different beam test period are listed for comparison. The values of a, b and c determined during this analysis are consistent with these other measurements.

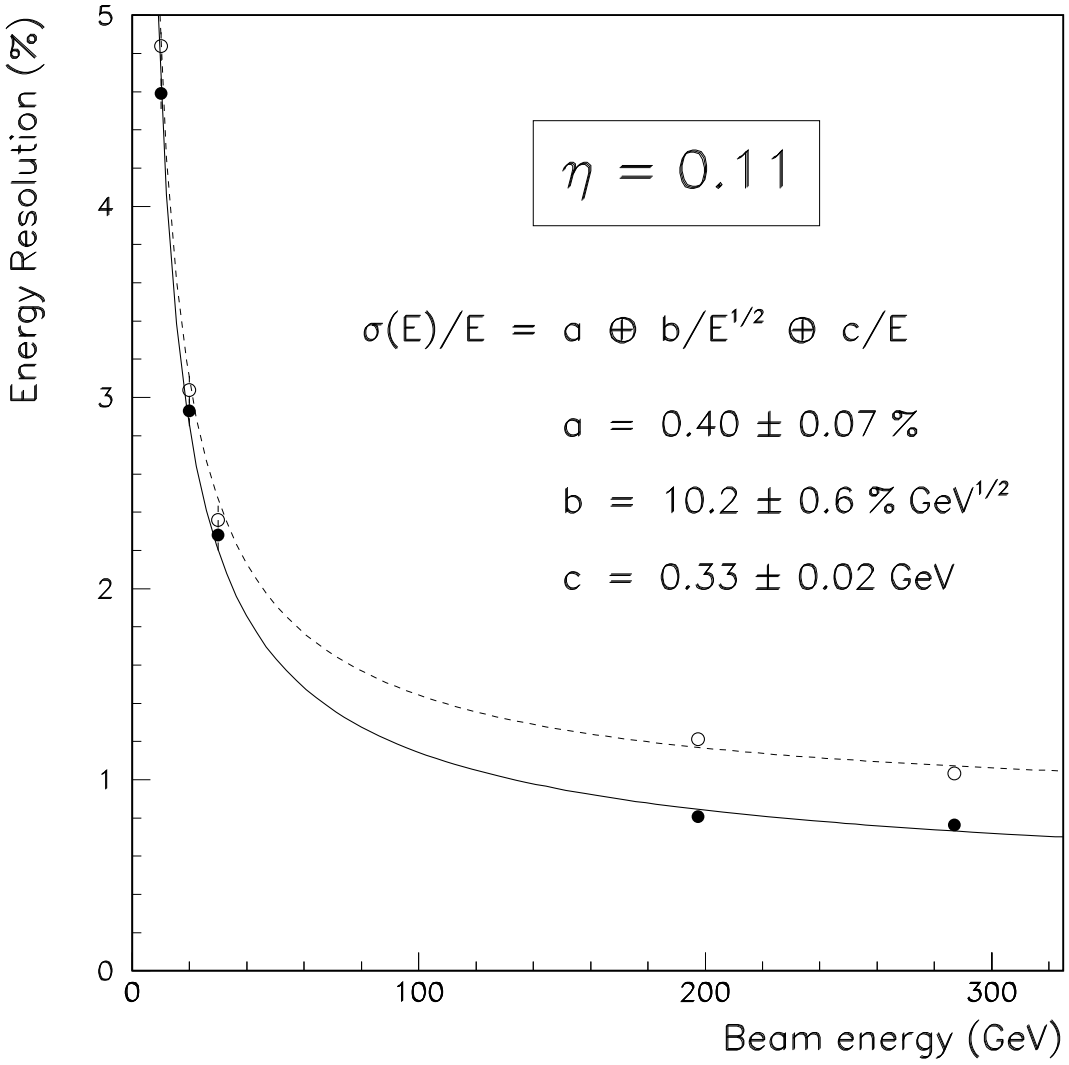

Figure 5.10: The electron energy resolution of the pointing geometry prototype. The measured values of the uncorrected (open circles) and corrected (closed circles) resolution are plotted for the available beam energies. The dashed curve is the best fit to the uncorrected energy resolution, while the solid curve describes the resolution after all correction have been applied. The values of a, b and c obtained for the corrected energy resolution are listed.

5.7 Uniformity and Large Scale Response Variations

The energy resolution described in section 5.6 is the average resolution measured over a single cell of the calorimeter. Contributions from the cell to cell response variations due to calibration errors and fluctuations in the average response with time are not included in these results. These effects were corrected for in previous sections by normalizing the average energy in each cell to one on a run by run basis (see section 5.3). Cell to cell nonuniformities produce an additional contribution to the constant term describing the large scale energy resolution ($a_{\rm L}$) which is added in quadrature to the local constant term a:

$$a_{\rm L} = a \oplus a_{\rm C} \quad , \tag{5.8}$$

where $a_{\rm C}$ is the contribution from cell to cell response variations.

The large scale uniformity of the pointing geometry prototype was determined using 197.5 GeV electron data distributed over 30 cells in Si sectors 1 and 2. Three cells in this region with pathological behavior attributed to faulty preamplifiers were excluded. Cluster weighting and impact position corrections were applied to the data in the remaining 27 cells and the energy spectrum of the combined data was obtained. The large scale resolution was determined by fitting the energy response of this data sample with a Gaussian function in the region of the energy peak excluding the low energy tail (see section 5.3). The local resolution was measured for the same data sample by applying a cell to cell normalization and measuring the width as before. The contribution to the resolution due to cell to cell response variations was then calculated by quadratically unfolding the local energy resolution from the large scale resolution. These cell to cell response variations were found to contribute $0.61\% \pm 0.05\%$ to the constant term of the resolution. The energy spectra of 197.5 GeV electron events obtained before and after applying cell by cell normalization are shown in figure 5.11.

As a crosscheck to this measurement, the cell to cell response variation was estimated

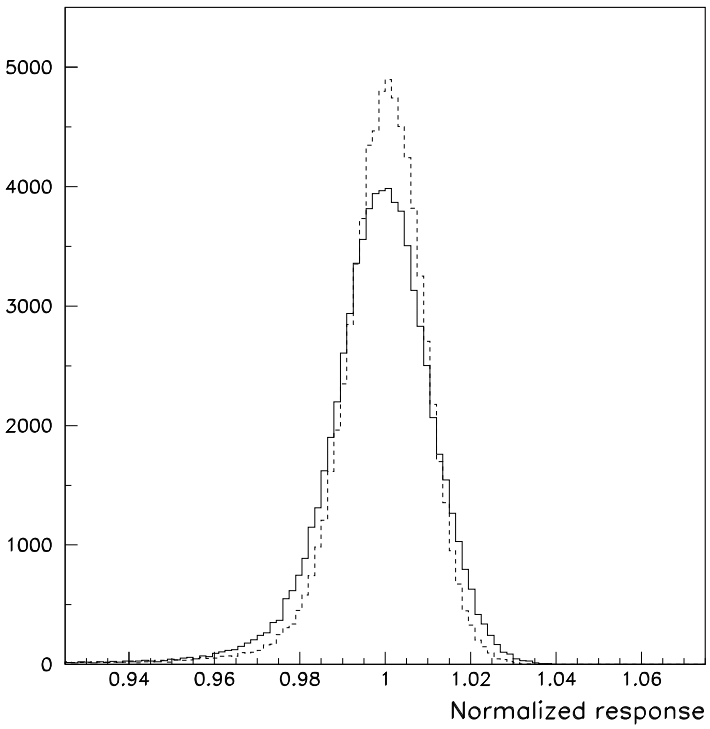

Figure 5.11: The normalized energy spectrum of 197.5 GeV electrons distributed over 27 calorimeter cells before (solid line) and after (dashed line) correcting for cell to cell response variations.

by computing the rms of the the distribution of mean energies measured in the 27 cells. This value was found to be $0.64\% \pm 0.05\%$, which is in good agreement with the value obtained previously. Assuming that these values represent the cell to cell response non-uniformity at all energies, the large scale constant term is found to be:

$$a_{\mathrm{L}} = (0.61\% \pm 0.05\%) \oplus (0.40\% \pm 0.07\%) = 0.73\% \pm 0.06\% \quad . \tag{5.9}$$

This large scale constant term clearly surpasses the ATLAS requirements of 1%, and the cell to cell nonuniformity of $0.61\% \pm 0.05\%$, which will affect first level trigger decisions, is also at an acceptable level. The effect of the large scale response non-uniformity on the energy

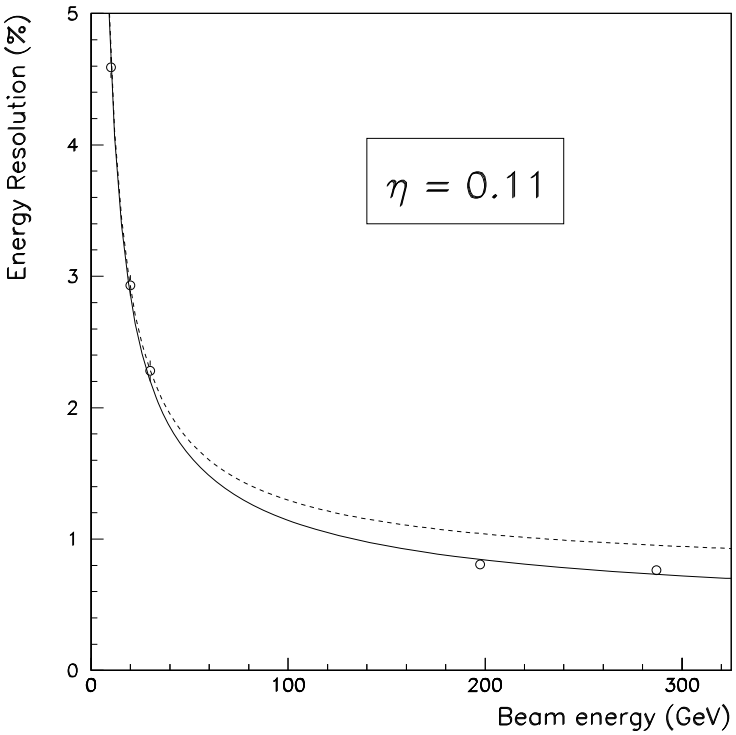

Figure 5.12: Effect of the cell to cell response non-uniformity on the large scale energy resolution. The solid line represents the corrected local energy resolution, and the dashed line is the resolution that would be measured over large areas of the calorimeter given a cell to cell non-uniformity of 0.61%.

resolution is illustrated in figure 5.12 where $a_c = 0.61\%$ and the local energy resolution is described by the corrected resolution from section 5.6. Response nonuniformity can be seen to significantly affect the energy resolution at high energies, where the constant term is dominant.

Chapter 6

Conclusions

The LHC to be built at CERN will provide the opportunity to explore the origin of mass at the electroweak scale and to search for new physics beyond the SM. The RD3 collaboration has constructed and tested a number of prototype calorimeters intended for use in the ATLAS detector at the LHC. A pointing accordion geometry LAr electromagnetic calorimeter prototype was tested at the CERN SPS in the spring and autumn of 1993 where it was exposed to electron beams ranging in energy from 10 GeV to 287 GeV. An analysis of this data was performed in order to assess the electron energy resolution of this prototype.

The energy of electron events corresponding to an average η of 0.11 was reconstructed using a weighted sum of the energy deposited in a 3×3 cluster of cells in each of the three longitudinal compartments of the calorimeter. The values of the weighting parameters were adjusted to optimize the energy resolution at all available beam energies, resulting in

$$E \propto (E_1 + \beta(E_2 + \gamma E_3)) \qquad , \tag{6.1}$$

where E is the reconstructed shower energy, E_i is the energy measured in the i_{th} sampling, $\beta = 0.93$, $\gamma = 1.0$ for $E_{\rm beam} > 10$ GeV and $\gamma = 0.0$ for $E_{\rm beam} = 10$ GeV. The change in the weight of the rear compartment at low energies was justified on the basis of the electronics

noise in this compartment.

The position dependence of the calorimeter energy response was found to have an rms of $0.69\% \pm 0.03\%$ in the η direction and $0.61\% \pm 0.03\%$ in the ϕ direction. In the η direction, this response was attributed to clustering effects and could be easily reduced to the level of 0.3% by applying a position dependent correction. The ϕ dependent response was found to be more complicated due to the accordion structure of a readout cell. Position dependent corrections to the response in ϕ direction also produced a residual position dependent response with an rms of $\sim 0.3\%$, and was limited by cell to cell variations in the ϕ dependent response. Improvements in the beam chamber positioning system and a more uniform distribution of electron events over the area of a readout cell in future tests would lead to further understanding of the position dependent response.

After cluster weighting and position dependent response corrections were applied, the local (over one cell) electron energy resolution corresponding to an average pseudorapidity of $\eta = 0.11$ was found to be described by

$$\frac{\sigma(E)}{E} = (0.40 \pm 0.07)\% \oplus \frac{(10.2 \pm 0.6)\%}{\sqrt{E}} \oplus \frac{0.33 \pm 0.02}{E} \quad , \tag{6.2}$$

where E is in GeV. Cell to cell response variations were found to contribute $0.61\% \pm 0.05\%$ to the local energy resolution yielding a large scale constant term of $0.73\% \pm 0.06\%$. These values, obtained with a $\sim$ 35 ns readout time, were shown to be consistent with other results reported for this prototype [35], and compare favourably with the ATLAS requirements of $1.0\% \oplus 10.0\%/\sqrt{E}$. The results of this work demonstrate that electromagnetic calorimetry meeting LHC performance specifications can be accomplished using a liquid argon calorimeter with a pointing accordion geometry.

Bibliography

[1] The LHC Study Group, *Design Study of the Large Hadron Collider (LHC)*, CERN/91-03, 2 May 1991.

[2] ATLAS Collaboration, *Letter of Intent*, CERN/LHCC/92-4, LHCC/I 2, 1 October 1992.

[3] The following institutes are members of the RD3 Collaboration: *University of Alberta, Canada; LAPP, Annecy, France; Univ. Autònoma Barcelona, Bellaterra, Spain; Brookhaven National Laboratory, Upton, USA; CERN, Geneva, Switzerland; DAPNIA-SPP Saclay, Gif-sur-Yvette, France; ISN, Grenoble, France; Univ. Autònoma Madrid, Spain; CPP Marseille, France; Dipartimento di Fisica dell'Università e Sezione INFN, Milano, Italy; Université de Montréal, Canada; LAL, Orsay, France; LPNHE, Universités de Paris VI et VII, France; Royal Institute of Technology, Stockholm, Sweden; University of Victoria, Canada.*

[4] The RD3 Collaboration, *Liquid Argon Calorimetry with LHC-Performance Specifications*, CERN/DRDC/90-31, DRDC/P5, August 1990.

[5] The RD3 Collaboration, *Hadronic and Electromagnetic Liquid Argon LHC Prototype Calorimeter with Pointing Geometry*, CERN/DRDC/91-21, DRDC/P5-Add.1, March 1991.

[6] The RD3 Collaboration, *R&D for a Liquid Argon Preshower*, CERN/DRDC/92-40, DRDC/P5-Add.2, August 1992.

[7] The RD3 Collaboration, *Status Report and Further R&D for EM and Hadronic Calorimetry*, CERN/DRDC/93-4, January 1993.

[8] B.Aubert *et al.* (RD3 Collaboration), *Performance of a liquid argon electromagnetic calorimeter with an "accordion" geometry*, Nucl. Instr. Meth. **A309** (1991) 438-449.

[9] B.Aubert *et al.* (RD3 Collaboration), *Performance of a liquid argon accordion calorimeter with fast readout*, Nucl. Instr. Meth. **A321** (1992) 467-478.

[10] B.Aubert *et al.* (RD3 Collaboration), *Performance of a liquid argon electromagnetic calorimeter with a cylindrical accordion geometry*, Nucl. Instr. Meth. **A325** (1993) 116-128.

[11] B. Aubert *et al.* (RD3 Collaboration), *Performance of a Liquid Argon Preshower Detector Integrated with an Accordion Calorimeter*, Nucl. Instr. Meth. **A330** (1993), 405-415.

[12] D. M. Gingrich *et al.* (RD3 Collaboration), *Performance of a Liquid Argon Accordion Hadronic Calorimeter Prototype*, to be submitted to Nucl. Instr. Meth.

[13] ATLAS Collaboration *Progress Report on ATLAS Milestones*, CERN/LHCC/93-51, 15 October 1993.

[14] For a discription of these processes see: W.R. Leo, *Techniques for Nuclear and Particle Physics Experiments*, (2nd Ed.), (Springer-Verlag New York, 1994).

[15] Particle Data Group, *Review of Particle Properties*, Phys. Rev. D: Particles and Fields, **45D** (1992).

[16] Richard Wigmans, *Advances in Hadron Calorimetry*, CERN-PPE-91-39, 1991.

[17] Ugo Amaldi, *Fluctuations in Calorimetry Measurements*, Physica Scripta **23** (1981) 409-424.

[18] T. Doke *et al. Average Energy Expended per Ion Pair in Liquid Argon*, Phys. Rev., **A9** (1974), p.1438.

[19] C. de La Taille, *Electronic Noise in LAr Calorimetry*, RD3 Note 45, 5 May 1993.

[20] F. Halzen and A. D. Martin *Quarks and Leptons: An Introductory Course in Modern Particle Physics*, (John Wiley and Sons, New York, 1984).

[21] N. Cabibbo, *Unitary Symmetry and Leptonic Decay*, Phys. Rev. Lett. **10** (1963), p.531; M. Kobayashi and T. Maskawa, *CP-Violation in the Renormalizable Theory of Weak Interactions*, Prog. Theor. Phys., **49**, (1973), p.652.

[22] F. Abe *et al. Evidence for Top Quark Production in* $\bar{p}p$ *Collisions at* $\sqrt{s} = 1.8$ *TeV*, FERMILAB-PUB-91/097-E.

[23] S. L. Glashow, *Partial-Symmetries of Weak Interactions*, Nucl. Phys., **22** (1961), p. 579; A. Salam in *Elementary Particle Theory*, ed. N. Svartholm, (Almquist and Wiksell, Stockholm, 1968); S. Weinberg, *A Model of Leptons*, Phys. Rev. Lett., /bf 19 (1967), p.1264.

[24] P. W. Higgs, *Spontaneous Symmetry Breakdown without Massless Bosons*, Phys. Rev., **145** (1966), p.1156.

[25] G. Arnison *et al.*, *Experimental Observation of Isolated Large Transverse Energy Electrons with Associated Missing Energy at* $\sqrt{s} = 540$ *GeV*, Phys. Lett. 122B (1983) 103.

[26] M. Banner *et al.*, *Observation of Single Isolated Electrons of High Transverse Momentum in Events with Missing Transverse Energy at the CERN* $p\bar{p}$ *Collider*, Phys. Lett. 122B (1983) 476.

[27] G. Arnison *et al.*, *Experimental Observation of Lepton Pairs of Invariant Mass Around 95* GeV/c^2 *at the CERN SPS Collider*, Phys. Lett. 126B (1983), 398.

[28] P. Bagnaia, *Evidence for* $Z^0 \rightarrow e^+e^-$ *at the CERN* $p\bar{p}$ *Collider*, Phys. Lett. 129B (1983) 130.

[29] J. R. Carter, *Precision tests of the Standard Model at LEP*, Proceedings of the Joint International Lepton-Photon Symposium and Europhysics Conference on High Energy Physics , Geneva, Switzerland, 25 July - 1 August 1991, World Scientific.

[30] P. Jenni and J. White, *Physics and Experimental Challenge of Future Hadron Colliders*, Proceedings of the 1993 Lake Louise Winter Institute, held in Lake Louise, Alberta, Canada, 21-27 Febuary 1993.

[31] Daniel Froidevaux, *Top Quark Physics at LHC/SSC*, CERN/PPE/93-148, 24 June 1993.

[32] R. Brun *et al.*, GEANT3 CERN DD/EE/84-1 (1987).

[33] The ATLAS Collaboration, *Impact of the bunch spacing scheme on the ATLAS detector and its performance*, ATLAS Note GEN-NO-001, 25 January 1993.

[34] V. Radeka and S. Rescia, *Speed and noise limits in ionization chamber calorimeters*, Nucl. Instr. Meth. **A265** (1988) 228-242.

[35] Andrea Cravero and Fabiola Gianotti, *Uniformity of response and energy resolution of a large scale prototype of the Barrel Accordion calorimeter* ATLAS Internal Note, CAL-NO-33, RD3 Note 54, 11 April 1994.

[36] B. Yu and V. Radeka, BNL 52444 (1990).

[37] D. Camin *et al.*, *Frontend in Gallium Arsenide*, Nucl. Instr. Meth. **A315** (1992) p.385.

[38] R. L. Chase, C. de La Taille, N. Seguin-Moreau, *Experimental results on cable-coupled preamplifiers (0T)*, Nucl. Instr. Meth. **A343** (1994) 598-605.

[39] J. S. White, *Spatial Reconstruction of Electrons with an Accordion Geometry Electromagnetic Calorimeter*, Masters thesis, University of Victoria, 1993.

[40] M. Lefebvre, G. Parrour and P. Pétroff, *Electromagnetic Liguid Argon Accordion Calorimeter Simulation*, RD3 note 41, (1993).